AWARD NUMBER: W81XWH-19-1-0110

TITLE: Modeling Ataxia - Telangiectasia with Induced Pluripotent Stem Cell-Derived Purkinje Cells

PRINCIPAL INVESTIGATOR: Mary E. Hatten

CONTRACTING ORGANIZATION: The Rockefeller University, New York, NY

REPORT DATE: May 2021

TYPE OF REPORT: Annual

PREPARED FOR: U.S. Army Medical Research and Development Command
Fort Detrick, Maryland 21702-5012

REPORT DOCUMENTATION PAGE

Form Approved
OMB No. 0704-0188

1. REPORT DATE	**2. REPORT TYPE**	**3. DATES COVERED**
May 2021	Annual	01Apr2020-31Mar2021

4. TITLE AND SUBTITLE

Modeling Ataxia - Telangiectasia with Induced Pluripotent Stem Cell-Derived Purkinje Cells

5a. CONTRACT NUMBER
W81XWH-19-1-0110

5b. GRANT NUMBER PR182292

5c. PROGRAM ELEMENT NUMBER

6. AUTHOR(S) Mary E. Hatten

E-Mail: hatten@rockefeller.edu

5d. PROJECT NUMBER 0011299708

5e. TASK NUMBER

5f. WORK UNIT NUMBER

7. PERFORMING ORGANIZATION NAME(S) AND ADDRESS(ES

Rockefeller University
New York, NY

8. PERFORMING ORGANIZATION REPORT NUMBER

9. SPONSORING / MONITORING AGENCY NAME(S) AND ADDRESS(ES)

U.S. Army Medical Research and Development Command
Fort Detrick, Maryland 21702-5012

10. SPONSOR/MONITOR'S ACRONYM(S)

11. SPONSOR/MONITOR'S REPORT NUMBER(S)

12. DISTRIBUTION / AVAILABILITY STATEMENT

Approved for Public Release; Distribution Unlimited

13. SUPPLEMENTARY NOTES

14. ABSTRACT

The purpose and scope of this research is to generate a model system to study human ataxia-telangiectasia patient Purkinje cells and define molecular differences between induced pluripotent stem cell (iPSC)-derived Purkinje cells (PCs) from patients, from unaffected siblings, and from mouse PCs. Major findings include analysis of patient and control iPS lines, differentiation to mature PCs, and initial morphological characterization as well as publication of our studies defining the model system. Patient cells did not display ATM kinase response to DNA damage in either the pluripotent state or the differentiated state, confirming their designation as patient cells. PCs from patient cells were found to have decreased soma size, nuclear size, nuclear circularity, and thinner primary dendrites. Ongoing experiments are examining gene expression and phosphoproteomics. Our model human pluripotent stem cell-derived PC model system, where gene signatures of human embryonic stem cell-derived PCs were compared to mouse PCs, was published in the *Proceedings of the National Academy of Sciences*.

15. SUBJECT TERMS

Induced Pluripotent Stem Cell; Purkinje Cell; Ataxia-Telangiectasia

16. SECURITY CLASSIFICATION OF:			**17. LIMITATION OF ABSTRACT**	**18. NUMBER OF PAGES**	**19a. NAME OF RESPONSIBLE PERSON**
a. REPORT	**b. ABSTRACT**	**c. THIS PAGE**			USAMRMC
Unclassified	Unclassified	Unclassified	Unclassified	20	**19b. TELEPHONE NUMBER** *(include area code)*

TABLE OF CONTENTS

	Page
1. Introduction	4
2. Keywords	4
3. Accomplishments	4-6
4. Impact	6
5. Changes/Problems	6-7
6. Products	7-8
7. Participants & Other Collaborating Organizations	8-9
8. Special Reporting Requirements	9
9. Appendices	9-20

1. INTRODUCTION:

Ataxia-telangiectasia (A-T) is a multisystem disorder caused by null mutations in the ATM gene, resulting in a variety of phenotypes, including telangiectasia, and ataxia caused by cerebellar dysfunction and degeneration, for which there is no cure. The ATM gene product, ATM, is a serine/threonine protein kinase with roles in a number of cellular processes, notably pathways involved in DNA repair. The most prominent cerebellar defects in A-T patients are seen in Purkinje cells (PC), including developmental defects as well as degeneration. To date, mouse models of A-T have not recapitulated PC phenotypes seen in A-T patients, and it has not been possible to define molecular differences between mouse models and human post-mortem tissue. To overcome these obstacles, we will develop a human model system to study A-T using a novel protocol we developed to differentiate induced pluripotent stem cells (iPSCs) derived from A-T patients into PC's. The overarching goal of this research is to define molecular differences between A-T human iPSC-PCs, unaffected human iPSC-PCs, and mouse PCs.

2. KEYWORDS

Induced Pluripotent Stem Cell; Purkinje Cell; Ataxia-telangiectasia

3. ACCOMPLISHMENTS

Major Goal 1: To generate six lines of iPSCs from A-T patients and unaffected, control patients and differentiate them into cerebellar Purkinje cells. The timeline for this milestone was 6-9 months and this goal is 66% complete.

Major Goal 2: To assess differences in gene expression and protein phosphorylation between A-T patient and unaffected iPSC-PCs. The timeline for this milestone was 14 months and this goal is ~50% complete.

The Major activities for this reporting period had three main goals: 1. Analysis of patient and control induced pluripotent stem cell (iPSC) lines, 2. Differentiation and morphological characterization of patient and control iPSC-PCs, and 3. Generation of cells for phosphoproteomic, transcriptomic, electron microscopic, and electrophysiological analysis.

Our first major goal was to further characterize iPSC lines generated during the previous reporting period. We had generated three control (family control) iPSC lines and two patient iPSC lines. One patient fibroblast line was refractory to reprogramming, likely due to advanced passage number of the starting cell line. Additional attempts to reprogram this line were unsuccessful. Of the lines generated, the three control and one patient iPSC line displayed a normal karyotype while one patient iPSC line was found to have an abnormal karyotype in all clones analyzes (7 clones). Assessment of the starting fibroblast line for this abnormal patient iPSC line found 50% of cells contained non-clonal abnormal karyotypes. This fibroblast line was also at a relatively higher passage number when delivered from the cell bank and likely picked up DNA rearrangements due to the absence of ATM, well known for its role in DNA damage repair. Unfortunately, earlier passage patient fibroblast cells are unavailable from the Coriell cell bank. We are proceeding with our experiments using the karyotypically normal family control and patient iPSC lines we have derived. Beyond the scope of this funding, we plan to obtain early passage patient fibroblasts from a collaborator in the field to add to the robustness of our studies.

We next sought to assess the ability of control and patient iPSCs to respond to DNA damage through ATM kinase signaling. A robust immunofluorescence assay was employed using a phosphospecific antibody of the ATM target KAP1. Upon DNA damage, in this case induced by neocarzinostatin, ATM rapidly phosphorylates serine 824 of KAP1. We observed strong phospho-KAP1 labeling following DNA damage in control, but not patient iPSCs. These results confirm the A-T patient status of our cell line.

To test the ability of control and A-T iPSC lines to generate cerebellar PCs, we differentiated the cells following a protocol developed by our lab (see attached publication). An important first test was whether our not our patient cell line would differentiate into PCs and survive so that the cells could be studied. We found no obvious differences between control and patient iPSCs in their ability to differentiate into post-mitotic (PCP2+) PCs after 24 days of differentiation. Following iPSC-PC enrichment by immunopanning and magnetic activated cell sorting, co-culture with mouse cerebellar glia for two months and mouse cerebellar granule cells for one month promoted maturation (Day +95 after isolation, Day 119 since the beginning of differentiation). Mature PCs at this timepoint similarly lack KAP1 phosphorylation in response to DNA damage (Fig. 1A). Compared to control cells, patient iPSC-PCs had significantly smaller cell soma, nuclei, altered nuclear circularity, and thinner primary dendrites. These findings suggest that A-T patient iPSC-PCs after 119 days of differentiation begin to exhibit characteristic changes in morphology associated with the disease (Figure 1). The finding that patient cells survive to this point and display altered morphology suggests that this is a useful timepoint to interrogate the phosphoproteome and transcriptome.

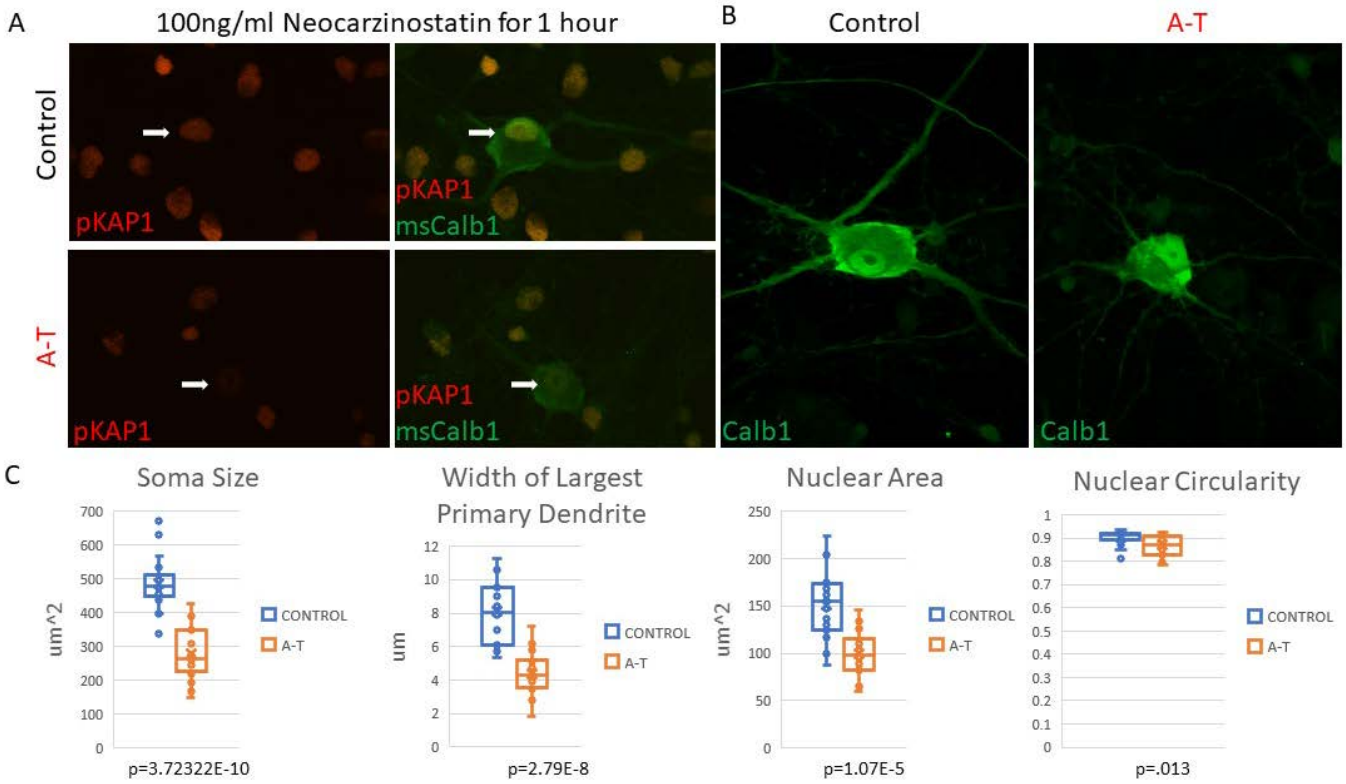

Figure 1. Characterization of control and A-T iPSC-PCs after +95 days of differentiation. **A.** Immunolabeling for phosphoKAP1 (pKAP1) following DNA damage. **B.** Representative images of control and A-T PC morphology by Calbindin1 (Calb1) immunofluorescence. **C.** Quantification of significant morphological differences between control and A-T iPSC-PCs. Statistical significance was determined using Student's T-test.

Ongoing activities are focused on generating sufficient cells for downstream analyses. These include planned phosphoproteomic and transcriptomic analyses. In particular, phosphoproteomic analyses require a large number of cells. Several large batches of cells are currently differentiating. Given our findings that A-T patient iPSC PCs have changes in morphology, we plan to also examine changes at the level of electron microscopy. Electrophysiology will be assessed using genetically encoded calcium and voltage indicators, as well as through conventional patch-clamp electrophysiology. Cells are currently differentiating for these experiments.

What opportunities for training and professional development has the project provided?
Several opportunities for training and professional development were provided by the project for David Buchholz, the lead Post-Doctoral Associate working on the project. One-on-one mentorship in the A-T field was provided by interactions with a leader in the field Dr. Yosef Shiloh, who discovered the causative A-T gene, *ATM*. The work funded by this DoD grant led to the awarding of the National Ataxia Foundation Young Investigator award for David Buchholz. This career development award is designed to encourage young clinical and scientific investigators to pursue a career in the field of Ataxia research.

How were the results disseminated to communities of interest?
Preliminary results were presented to the tri-institutional stem cell forum, a weekly meeting between stem cell researchers at The Rockefeller University, Weill Cornell Medical College, and Memorial Sloan Kettering Institute. Dissemination of results was somewhat limited during the past year due to Covid, which precluded attendance of the PI and Dr. Buchholz at the Society for Neuroscience meeting as well as other regional meetings.

What do you plan to do during the next reporting period to accomplish the goals?
Over the final reporting period we plan to continue differentiation experiments to generate phosphoproteomic and gene expression data to compare control iPSC-PCs to patient iPSC-PCs. The main goal of these experiments will be to define phenotypic differences between control and patient PCs.

4. IMPACT

What was the impact on the development of the principal discipline(s) of the project?
The goal of this project is to use induced pluripotent stem cells (iPSCs) to study ataxia-telangiectasia (A-T). During the reporting period, we were able to show that iPSCs from patients with A-T can differentiate into mature Purkinje cells (PCs) that show differences in morphology compared to controls. This work has created the first model system to study human A-T patient PCs and defined initial characteristics of this system that are consistent with known alterations in PCs in A-T patients. The cell lines generated by our work as well as the model system will be a powerful approach to study this devastating disease, especially given reports in the literature that mice mutant for the A-T gene, *Atm*, do not display the same PC phenotype as A-T patients.

What was the impact on other disciplines?
Nothing to report.

What was the impact on technology transfer?
Nothing to report.

What was the impact on society beyond science and technology?
Nothing to report.

5. CHANGES/PROBLEMS

Two patient fibroblasts lines contained a large number of cells with karyotype abnormalities, making them unsuitable for use. These issues are discussed further below.

Changes in approach and reasons for change
No major changes in approach were taken.

Actual or anticipated problems or delays and actions or plans to resolve them
As discussed above, two patient fibroblast lines obtained from the cell bank at the Coriell Institute for Medical Research were at a high passage number (>10 passages) and contained >50% of cells with non-clonal karyotype abnormalities. This resulted in two issues. For the highest passage cell line, no iPSC clones could be generated. Increased passage number, even with healthy fibroblast lines, is well known to decrease the efficiency of iPSC reprogramming. For a second cell line, while iPSC clones were derived, none of the 8 clones that we karyotyped had a normal karyotype. This is likely due to the starting fibroblasts having a large percentage of non-clonal karyotype abnormalities. This accumulation of karyotype abnormalities is likely related to the A-T patient status, as the underlying gene, *ATM*, is involved in DNA damage repair. Therefore, it is essential to obtain earlier passage cells both for ease of reprogramming and to avoid karyotype abnormalities. Unfortunately, for these patient cell lines, no earlier passage cells exist at the Coriell Institute. Given this, we are moving forward with the single karyotypically normal control and patient iPSC lines that we have generated as these lines will still give valuable information and rescue of the patient iPSC line with CRISPR will provide a rigorous confirmation. Outside the scope of this current funding, we are also receiving additional control and patient iPSC lines from our collaborator Dr. Shiloh for future study.

Changes that had a significant impact on expenditures
No changes had a significant impact on expenditures.

Significant changes in use or care of human subjects, vertebrate animals, biohazards, and/or select agents

Significant changes in use or care of human subjects
No human subjects were used in this project.

Significant changes in use or care of vertebrate animals
No significant changes in use or care of vertebrate animals.

Significant changes in use of biohazards and/or select agents
No significant changes in use of biohazards and/or select agents.

6. PRODUCTS

Publications, conference papers, and presentations

Journal publications.

Buchholz DE, Carroll TS, Kocabas A, Zhu X, Behesti H, Faust PL, Stalbow L, Fang Y, Hatten ME. (2020). “Novel Genetic Features of Human and Mouse Purkinje Cell Differentiation Defined by Comparative Transcriptomics.” *Proceedings of the National Academy of Sciences.* 117(26):15085-15095.

Acknowledgement of federal support: Yes

Books or other non-periodical, one-time publications.
Nothing to report.

Other publications, conference papers and presentations.
Presentation to the Tri-I Stem Cell Forum, a weekly meeting between stem cell researchers at The Rockefeller University, Weill Cornell Medical College, and Memorial Sloan Kettering Institute.

Website(s) or other Internet site(s)
Nothing to report.

Technologies or techniques
Nothing to report.

Inventions, patent applications, and/or licenses
Nothing to report.

Other Products
Nothing to report.

7. PARTICIPANTS & OTHER COLLABORATING ORGANIZATIONS

What individuals have worked on the project?
Name: Mary E. Hatten
Project Role: PD/PI
Researcher Identifier (e.g. ORCID ID): 0000-0001-9059-660X
Nearest person month worked: 1.2

Contribution to Project: Dr. Hatten designed and analyzed experiments.
Funding Support: See below (Complete only if the funding support is provided from other than this award.)

Name: David E. Buchholz
Project Role: Post-doctoral Associate
Researcher Identifier (e.g. ORCID ID): 0000-0003-4021-7696
Nearest person month worked: 12

Contribution to Project: Dr. Buchholz designed, performed, and analyzed experiments.
Funding Support: See below

Has there been a change in the active other support of the PD/PI(s) or senior/key personnel since the last reporting period?

(NEW) 1 R01 NS116089-01A1 12/05/2020-11/30/2025
Funding Agency: NIH NINDS Annual Direct Costs to Hatten Lab
Title: Role of ASTN2 in cerebellar circuit function and ASD-related behaviors
Hatten effort: 1.2 Cal. Months

(NEW) 1 R21 NS121438-01 Hatten (PI) 04/01/21-09/30/22 1.2 calendar
Funding Agency: NIH NINDS
Title: Molecular Mechanisms of Purkinje Cell Degeneration in Ataxia-Telangiectasia

(NEW) NAF Young Investigator Award Buchholz (PI) 03/01/21-02/28/22 0.6 calendar
Funding Agency: National Ataxia Foundation
Title: Molecular Mechanisms of Human Purkinje Cell Degeneration in Ataxia-Telangiectasia

5 R21 NS114545-02 Hatten (PI) 09/01/19-8/31/2 1.2 calendar
Funding Agency: NIH NINDS
Title: Chromatin Changes During CNS Migration and Circuit Formation
Role: PI

(CLOSED) Robertson Therapeutics Development Fund Hatten (PI)
03/01/20 – 2/29/21 0.6 calendar
Funding Agency: RTDF

(CLOSED) Funding Agency: A-T Children's Project Hatten (PI)
08/01/18-07/31/20 06. Calendar

What other organizations were involved as partners?
Nothing to report.

8. Special Reporting Requirements
Nothing no report.

9. APPENDICES
Our published manuscript is attached for reference.

Novel genetic features of human and mouse Purkinje cell differentiation defined by comparative transcriptomics

David E. Buchholz[a], Thomas S. Carroll[b], Arif Kocabas[a], Xiaodong Zhu[a], Hourinaz Behesti[a], Phyllis L. Faust[c], Lauren Stalbow[a], Yin Fang[a], and Mary E. Hatten[a,1]

[a]Laboratory of Developmental Neurobiology, The Rockefeller University, New York, NY 10065; [b]Bioinformatics Resource Center, The Rockefeller University, New York, NY 10065; and [c]Department of Pathology and Cell Biology, Columbia University Irving Medical Center and the New York Presbyterian Hospital, New York, NY 10032

Contributed by Mary E. Hatten, April 22, 2020 (sent for review January 3, 2020; reviewed by Lorenz Studer and Hynek Wichterle)

Comparative transcriptomics between differentiating human pluripotent stem cells (hPSCs) and developing mouse neurons offers a powerful approach to compare genetic and epigenetic pathways in human and mouse neurons. To analyze human Purkinje cell (PC) differentiation, we optimized a protocol to generate human pluripotent stem cell-derived Purkinje cells (hPSC-PCs) that formed synapses when cultured with mouse cerebellar glia and granule cells and fired large calcium currents, measured with the genetically encoded calcium indicator jRGECO1a. To directly compare global gene expression of hPSC-PCs with developing mouse PCs, we used translating ribosomal affinity purification (TRAP). As a first step, we used *Tg(Pcp2-L10a-Egfp)* TRAP mice to profile actively transcribed genes in developing postnatal mouse PCs and used metagene projection to identify the most salient patterns of PC gene expression over time. We then created a transgenic *Pcp2-L10a-Egfp* TRAP hPSC line to profile gene expression in differentiating hPSC-PCs, finding that the key gene expression pathways of differentiated hPSC-PCs most closely matched those of late juvenile mouse PCs (P21). Comparative bioinformatics identified classical PC gene signatures as well as novel mitochondrial and autophagy gene pathways during the differentiation of both mouse and human PCs. In addition, we identified genes expressed in hPSC-PCs but not mouse PCs and confirmed protein expression of a novel human PC gene, CD40LG, expressed in both hPSC-PCs and native human cerebellar tissue. This study therefore provides a direct comparison of hPSC-PC and mouse PC gene expression and a robust method for generating differentiated hPSC-PCs with human-specific gene expression for modeling developmental and degenerative cerebellar disorders.

human pluripotent stem cells | Purkinje cell | transcriptomics

Emerging evidence supports a role for the cerebellum in a wide range of cognitive functions, including language, visuospatial memory, attention, and emotion, in addition to classical functions in adaptive, feed forward motor control (1–3). Cerebellar defects therefore contribute to a broad spectrum of neurological disorders including ataxias, autism spectrum disorder (ASD), intellectual disability, and other cerebellar-based behavioral syndromes (2–7). As the sole output neuron of the cerebellar cortex, the Purkinje cell (PC) plays a key role in both development and function of the cerebellum, integrating information from their two primary inputs, cerebellar granule cells (GCs) and climbing fiber afferents (8). A loss of PCs is one of the most consistent findings in postmortem studies in patients with ASD (4), and specific targeting of PCs in mouse models of ASD-associated genes leads to impaired cerebellar learning (9) and social behaviors (6, 10). Notably, PC degeneration is also a hallmark of human spinocerebellar ataxias (7).

While modeling genetic disorders in mice has provided fundamental insights into disease mechanisms, human disease often cannot be fully recapitulated in the mouse. A prominent example is ataxia-telangiectasia, which shows massive loss of PCs in humans but not in the mouse (11). Human pluripotent stem cells (hPSCs) provide a complementary approach to studying human disease in the mouse (12–14). Validated methods to derive specific neural subtypes from hPSCs are necessary prerequisites to disease modeling. We and others have recently developed protocols to derive PCs from hPSCs (15–18).

One limitation of most hPSC-derived central nervous system (CNS) neurons is the lack of genetic information, especially of transcriptomic signatures, to rigorously identify specific types of neurons and to compare their development across species. Here, we present an optimized method to generate well-differentiated human pluripotent stem cell-derived Purkinje cells (hPSC-PCs) and use translating ribosomal affinity purification (TRAP) to directly compare global gene expression patterns of developing mouse PCs with that of differentiating hPSC-PCs. After induction with signals to generate PCs, purification, and coculture with cerebellar glia, hPSC-PCs formed synapses with mouse GCs and fired large calcium currents, measured with the genetically encoded calcium indicator jRGECO1a. Metagene projection

Significance

To compare global gene expression features of differentiating human pluripotent stem cell-derived Purkinje cells (hPSC-PCs) and developing mouse Purkinje cells (PCs), we derived hPSC-PCs and compared gene expression datasets from human and mouse PCs. We optimized a differentiation protocol that generated hPSC-PCs most similar in gene expression to mouse P21 PCs. Metagene projection analysis of mouse PC gene expression over postnatal development identified both classical PC marker genes as well as novel mitochondrial and autophagy gene pathways. These key gene expression patterns were conserved in differentiating hPSC-PCs. We further identified differences in timing and expression of key gene sets between mouse and hPSC-PCs and confirmed expression of a novel human PC marker, CD40LG, in human cerebellar tissue.

Author contributions: D.E.B., H.B., and M.E.H. designed research; D.E.B., A.K., X.Z., P.L.F., L.S., and Y.F. performed research; D.E.B., T.S.C., and M.E.H. analyzed data; and D.E.B. and M.E.H. wrote the paper.

Reviewers: L.S., Memorial Sloan Kettering Cancer Center; and H.W., Columbia University Medical Center.

The authors declare no competing interest.

Data deposition: Microarray data can be found in the Gene Expression Omnibus database (accession no. GSE140307). RNAseq data can be found in the Gene Expression Omnibus database (accession no. GSE140306).

[1]To whom correspondence may be addressed. Email: hatten@rockefeller.edu.

This article contains supporting information online at https://www.pnas.org/lookup/suppl/doi:10.1073/pnas.2000102117/-/DCSupplemental.

First published June 16, 2020.

analysis of global gene expression patterns revealed that differentiating hPSC-PCs share classical and developmental gene expression signatures with developing mouse PCs that include novel mitochondrial and autophagy gene pathways. Comparative bioinformatics of key gene pathways showed that hPSC-PCs closely match juvenile P21 mouse PCs, suggesting that they are relatively mature. Gene expression profiling also identified human-specific genes in hPSC-PCs. Protein expression for one of these human-specific genes CD40LG, a tumor necrosis factor superfamily member, was confirmed in both hPSC-PCs and native human cerebellar tissue. This study therefore provides a direct comparison between hPSC-PC and mouse PC gene expression.

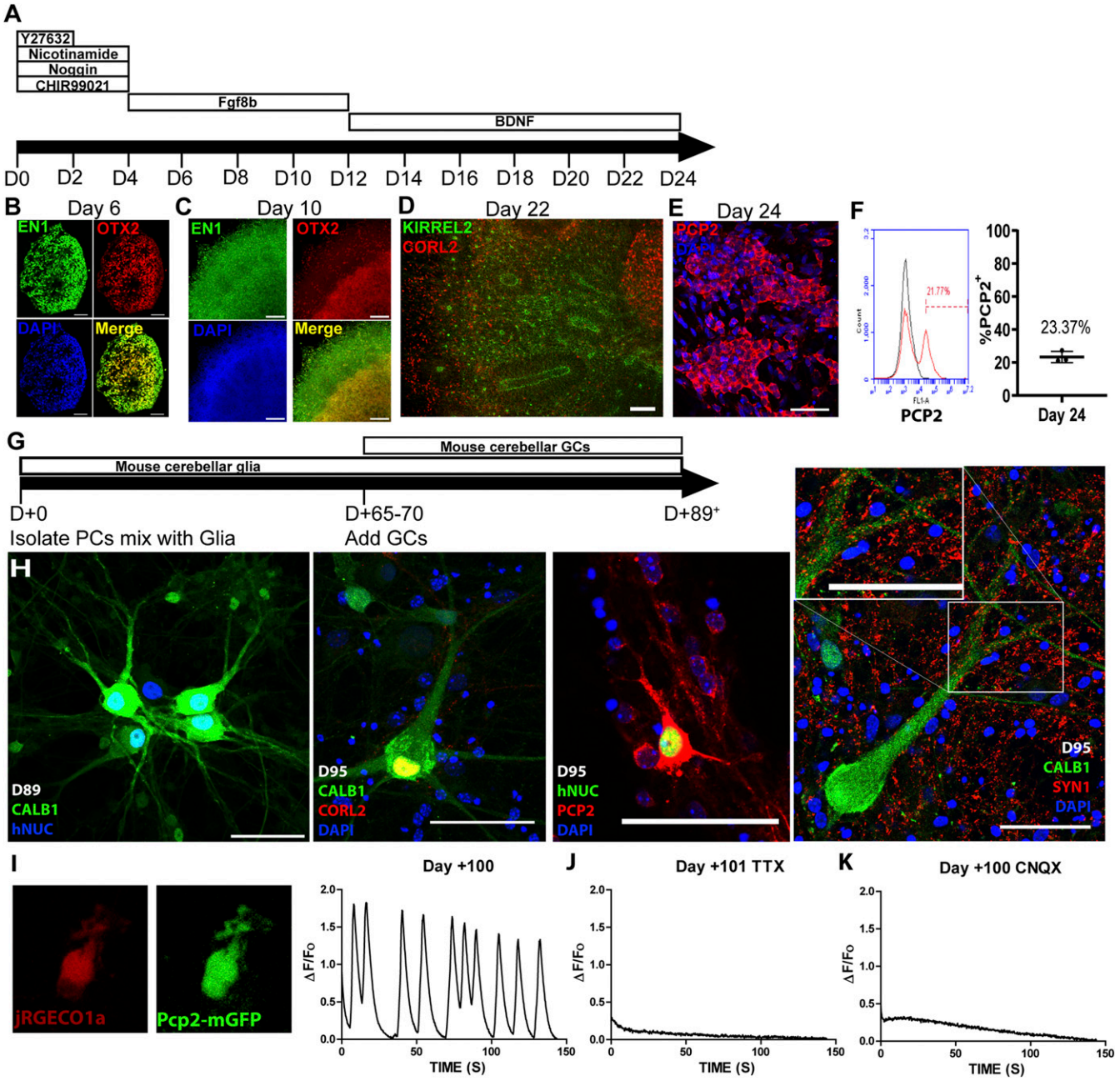

Fig. 1. Differentiation of hPSCs to PCs. (*A*) Schematic of the first phase of differentiation. (*B*) Immunolabeling of a cryosection of a representative neural aggregate after 6 d of differentiation; 10 μm *z* projection. (Scale bar: 50 μm.) (*C*) Immunolabeling of an attached neural aggregate after 10 d of differentiation; 18 μm *z* projection. (Scale bar: 100 μm.) (*D*) Immunolabeling of an attached neural aggregate after 22 d of differentiation; 18 μm *z* projection. (Scale bar: 100 μm.) (*E*) Immunolabeling of an attached neural aggregate after 24 d of differentiation. (Scale bar: 50 μm.) (*F*) A representative histogram and quantification of flow cytometry for PCP2 after 24 d of differentiation. Positive signal is >0.01% of secondary control. Error bars represent SD. (*G*) Schematic of the second phase of differentiation. (*H*) Immunolabeling of hPSC-PCs after isolation and coculture with mouse glia cells and GCs for an additional >89 d. The panels from left to right show 7 μm *z* projection, 5 μm *z* projection, 5 μm *z* projection, and single optical section. (Scale bars: 50 μm.) (*I*) Live imaging of genetically encoded calcium indicator jRGECO1a and hPSC-PC reporter Pcp2-mGFP after 100 d of coculture with mouse glia cells and GCs and a trace of the change in jRGECO1a fluorescence (ΔF/Fo) over time. (*J*) Representative trace of jRGECO1a fluorescence in the presence of the Na^+ channel antagonist TTX after 101 d of coculture with mouse glia cells and GCs. (*K*) Representative trace of jRGECO1a fluorescence in the presence of the glutamate receptor antagonist CNQX after 100 d of coculture with mouse glia cells and GCs.

Results

Differentiation of hPSCs to PCs. We previously reported a protocol to generate cerebellar PCs from hPSCs, which employed an approach that has proven broadly successful for hPSC differentiation: recapitulation of development through the addition of inductive signals (18, 19). Here, we have optimized that protocol, quantifying the effect of signaling molecules on early differentiation and introducing methods for isolation of immature PCs and coculture with mouse cerebellar glia cells and GCs. These additions provide a robust method for generation of hPSC-PCs.

Neural induction was achieved by culture of hPSC aggregates in NOGGIN (20) and nicotinamide (21, 22). Nicotinamide significantly decreased expression of the pluripotency marker *OCT4* while significantly increasing expression of the mid-/hindbrain neural tube markers *EN1* and *EN2* after 6 d of differentiation when combined with additional differentiation factors (Fig. 1*B* and *SI Appendix*, Fig. S1 *A* and *B*). Specific concentrations of GSK3β inhibitors such as CHIR99021 have previously been used to mimic developmental Wnt signaling gradients to direct hPSCs to specific rostral–caudal domains, giving rise to midbrain dopaminergic neurons (23–25). We confirmed that increasing concentrations of CHIR99021 led to progressive caudalization of neural tissue in our differentiation protocol, with a concentration of 1.5 μM generating the highest expression of cerebellar anlage markers *EN1*, *EN2*, and *GBX2* after 6 d when combined with additional differentiation factors (Fig. 1*B* and *SI Appendix*, Fig. S1 *A* and *B*). Following neural induction and initial rostral–caudal patterning, the cerebellum is subsequently specified by high levels of FGF8b signaling (8). We found that addition of 100 ng/mL FGF8b at day 4 of differentiation led to a significant increase in *EN1*, *EN2*, and *GBX2* expression at day 6 compared with 1 ng/mL FGF8b (Fig. 1*B* and *SI Appendix*, Fig. S1*A*). The addition of NOGGIN, nicotinamide, CHIR99021, and FGF8b at specific concentrations and times led to broad expression of EN1/OTX2 (Fig. 1*B* and *SI Appendix*, Fig. S1 *A* and *C*) and *GBX2* (*SI Appendix*, Fig. S1*A*), which may correspond to the earliest stages of midbrain/hindbrain specification when all genes are coexpressed (26). At this stage, ∼84% of cells coexpressed EN1/OTX2 (*SI Appendix*, Fig. S1*C*). After plating the hPSC aggregates on laminin at day 6 and continued culture in FGF8b, our cultures separated into $EN1^+/OTX2^+$ (midbrain) and $EN1^+/OTX2^-$ (hindbrain/cerebellum) regions (Fig. 1*C*). FGF8b was removed on day 12, and brain-derived neurotrophic factor (BDNF) was added to support postmitotic neurons. From day 12 to day 24, neural rosettes expressing the cerebellar ventricular zone marker KIRREL2 gave rise to increasing numbers of adjacent cells outside of the rosettes expressing the earliest postmitotic PC marker, CORL2/SKOR2 (Fig. 1*D*), similar to organization within the developing cerebellum (8). The definitive postmitotic PC marker PCP2 was observed starting at day 18 onward (Fig. 1*E*). Flow cytometry for PCP2 shows that ∼23% of cells express this marker at day 24 of differentiation (Fig. 1*F*).

To provide a more defined model system, we developed a two-step procedure to purify PCs after 22 to 28 d of differentiation: negative selection by GD3 immunopanning (27) and positive selection by NCAM1 magnetic cell sorting (*SI Appendix*, Fig. S1*D*). This procedure enriched PCs to ∼84% as quantified by $PCP2^+$/human nuclear antigen$^+$ ($hNUC^+$) immunolabeling at day +95 (*SI Appendix*, Fig. S1*E*). Since the maturation of mouse PCs is strongly dependent on cell–cell interactions with glia and cerebellar GCs (27), we first cocultured hPSC-PCs with cerebellar glia for 65 to 70 d followed by coculture with their presynaptic partner neurons, GCs, for 25 to 30 d (Fig. 1*G*). Culturing purified hPSC-PCs with glia prior to culture with GCs resulted in more robust expression of CALB1 than with culturing the cells with GCs alone (*SI Appendix*, Fig. S1*F*). In addition, after coculture with glia, hPSC-PCs cocultured with mouse GCs extended thick primary dendrites similar to those seen in developing human PCs (*SI Appendix*, Fig. S4*B*) and expressed other classical mouse PC marker genes, including CORL2/SKOR2, and PCP2 (Fig. 1*H*). Soma size was variable between ∼15 and 30 μm in diameter. Immunolabeling of pre- and postsynaptic proteins SYN1 and PSD-95 revealed numerous puncta along hPSC-PC dendrites, indicative of the formation of synapses between hPSC-PCs and GCs (Fig. 1*H* and *SI Appendix*, Fig. S1*G*) (28, 29). After ∼17 wk of differentiation, the morphology of hPSC-PCs resembled that of immature human fetal PCs after ∼18 to 25 wk of gestation (*SI Appendix*, Fig. S4*B*).

Functional Testing of hPSC-PCs with Genetically Encoded Calcium Indicators. To confirm the presence of functional synaptic connections between mouse GCs and hPSC-PCs, we nucleofected the genetically encoded calcium indicator jRGECO1a and PCP2-mGFP reporter vectors (30) into freshly purified hPSC-PCs (Fig. 1*I*). After coculture with mouse cerebellar glia for 70 d and GCs for an additional 30 d, several different calcium firing patterns were observed in labeled $Pcp2^+$ hPSC-PCs (Fig. 1*I* and *SI Appendix*, Fig. S1*I*, and Movies S1–S3). A slow decay of 30 to 90 s was observed in many responses, suggesting release of calcium from intracellular stores (*SI Appendix*, Fig. S1*I*). Signals greater than onefold change in fluorescence over baseline ($\Delta F/F_o$ were only observed in the presence of GCs, when SYN1/PSD-95^+ synapses had been observed between GCs and hPSC-PCs. We observed that ∼58% of measured PCs exhibited calcium transients $\Delta F/F_o > 0.3$, which has been observed as the average response of a single action potential in rat hippocampal neurons (30). hPSC-PC activity was inhibited by addition of the voltage-gated sodium channel antagonist tetrodotoxin (TTX) and by addition of the ionotropic glutamate receptor antagonist cyanquixaline (CNQX) (Fig. 1 *J* and *K*). Inhibition by CNQX is consistent with the formation of functional synapses between glutamatergic GCs and hPSC-PCs.

Determination of hPSC-PC Maturity by Comparative Transcriptomics. To examine the identity of hPSC-PCs at the transcriptome level and to compare global patterns of gene expression of differentiating hPSC-PCs with developing mouse PCs, we used TRAP to purify mRNAs (31). Lentiviral delivery of the L10a-EGFP tag under control of well-characterized *Pcp2* genetic elements (32, 33) generated a Pcp2-L10a-Egfp hPSC line (Fig. 2*A* and *SI Appendix*, Fig. S2 *A* and *B*). By immunofluorescence, L10a-EGFP expression was restricted to $PCP2^+$ hPSC cells that coexpressed the classical PC marker CALB1 (Fig. 2*A*). L10a-EGFP expression was never observed in PCP2-negative cells. L10a-EGFP properly localized to the soma and nucleolus, providing a convenient live tag for differentiating hPSC-PCs (Fig. 2*A* and *SI Appendix*, Fig. S2*B*) (34). At day 24, ∼44% of $PCP2^+$ cells expressed the L10-EGFP tag, as quantified by immunolabeling, suggesting partial silencing of the lentiviral construct, in agreement with prior reports of lentiviral transgenesis in hPSCs (*SI Appendix*, Fig. S2*C*) (35). Translating messenger RNA (mRNA) was affinity purified from hPSC-PCs after 24 d of differentiation and after coculture with mouse cerebellar glia and GCs for an additional +95 d and analyzed by RNAseq (Fig. 2*B*). Principal component analysis of RNAseq datasets from undifferentiated hPSC lines H1 and RUES2 and hPSC-PCs on day 24 or day +95 showed tight clustering within replicates and separation between groups (Fig. 2*C*).

To profile global gene expression patterns of mouse PCs at different stages of development, we used the *Tg(Pcp2-L10a-Egfp)* TRAP mouse line (*SI Appendix*, Fig. S2*D*). mRNAs were purified at P0, when mouse PCs are beginning to differentiate; at P7, when GCs are migrating and extending parallel fibers that synapse with nascent PCs; at P15, when PCs are maturing; at P21, when the cerebellar circuitry has formed and PC dendritic

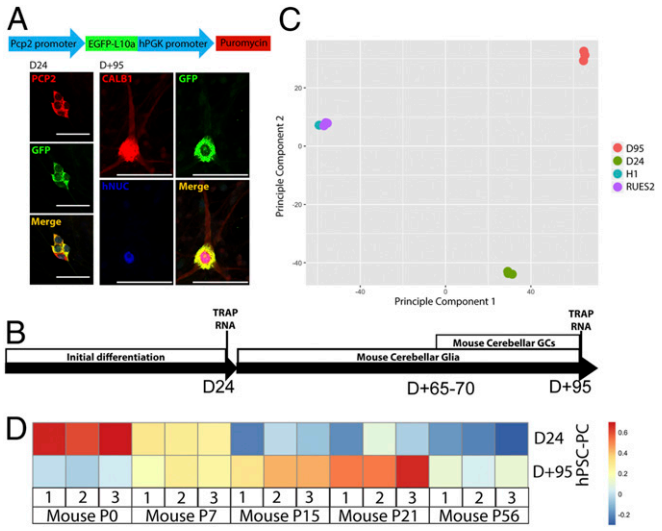

Fig. 2. Comparison of hPSC-PC gene expression with mouse PC gene expression over development. (*A*) Schematic of the lentiviral construct used to create the PCP2-EGFP-L10a TRAP hPSC line and immunolabeling of the construct in differentiating hPSC-PCs; 4 μm *z* projections. (Scale bars: 50 μm.) (*B*) Schematic depicting timing of TRAP RNA isolation from differentiation hPSC-PCs. (*C*) Principle component analysis of differentiating hPSC-PCs after 24 and +95 d as well as undifferentiated hESC lines (H1, RUES2). (*D*) Heat map showing median scaled ssGSEA enrichment scores of gene expression levels in mouse PCs over postnatal development for gene sets defined as $\log_2$ 4-fold (16-fold) change between day 24 and day +95 in hPSC-PCs. Day 24 hPSC-PCs are most similar to P0 mouse PCs ($P = 0.0014$). Day +95 PCs are most similar to P21 mouse PCs ($P = 1.74\text{x}10^{-32}$).

arbors are nearly mature; and at P56, when PCs are fully mature (*SI Appendix*, Fig. S4*A*). Isolated mRNA was analyzed by microarray (Dataset S1). Single-sample gene set enrichment analysis (ssGSEA) of RNAseq gene sets defined in hPSC-PCs were used to compare gene expression between species and platforms (36). Gene sets for hPSC-PC time points were defined as $\log_2$ 4-fold (16-fold) difference between day 24 and day +95 (Dataset S2). ssGSEA enrichment scores of hPSC-PC day 24 and day +95 gene sets were analyzed in mouse PC expression data (Fig. 2*D*). hPSC-PCs at day 24 were most similar to mouse PCs at P0 ($P = 0.0014$), while hPSC-PCs at day +95 were most similar to mouse PCs at P21 ($P = 1.74\text{x}10^{-32}$). For added stringency, we processed the data through an in silico combined human–mouse reference genome to subtract possible mouse reads and observed the same patterns (*SI Appendix*, Fig. S2*E*) (37). Defining gene sets in mouse PCs (100 highest-expressed genes per time point) and assessing expression levels in hPSC-PCs also gave the same pattern (*SI Appendix*, Fig. S2 *F* and *G*). These data indicate that at the transcriptome level, hPSC-PCs mature over differentiation to a stage most similar to juvenile mouse P21 PCs.

Nonnegative Matrix Factorization Defines Developmental PC Gene Signatures. To assess global transcription profiles of mouse PCs over postnatal developmental and identify key gene pathways, we used a nonnegative matrix factorization (NMF) approach to define clusters of genes with similar developmental expression patterns, termed metagenes (38–40). This method revealed several metagenes with high cophenetic correlation coefficients (*SI Appendix*, Fig. S3*A*). Of these, number 5 (five metagenes) had the lowest dispersion and was therefore used in this study (Fig. 3*A* and *SI Appendix*, Fig. S3*A*). We then identified gene ontology (GO) sets with a correlation coefficient >0.85 to any metagene (Fig. 3*B* and Dataset S3). GO terms associated with PC development were highly correlated with metagene 1 (Fig. 3*B* and *SI Appendix*, Fig. S3*B*), validating our NMF approach. The level of expression of PC developmental genes in this metagene set increased in mouse PCs from P0 to P7 and also, in hPSC-PCs from day 24 to day +95. Thus, at the transcriptome level, hPSC-PCs expressed gene sets that identify developing mouse PCs.

At P0, mouse PCs highly expressed gene sets associated with GO terms for axon outgrowth. These gene sets correlated with metagene 3, showing high expression at P0 but then dropping off at P7 and further dropping at P56 (Fig. 3*B* and *SI Appendix*, Fig. S3*B*). The patterns for axon outgrowth similarly decreased in hPSC-PCs from day 24 to day +95. Developmental gene signatures for mitochondria and autophagy GO terms correlated highly with metagenes 1 and 5, showing a sharp increase in expression from P0 to P7 (Fig. 3*B* and *SI Appendix*, Fig. S3*B*). Both signatures similarly showed increases in expression in hPSC-PCs from day 24 to day +95. Expression patterns of representative genes for each of the GO categories from Fig. 3*B* are shown in Fig. 3*C*. In summary, we observed P0 to P7 to be a highly dynamic period for PC gene expression, showing down-regulation of axon outgrowth genes and up-regulation of mitochondria, autophagy, and classical PC marker genes. These gene expression dynamics were conserved in hPSC-PCs from day 24 to day +95.

Differences between hPSC-PCs and Mouse PCs. Three types of differences in gene expression patterns were observed between mouse PCs and hPSC-PCs. First, the timing of expression of some gene pathways was delayed in hPSC-PCs. Notably, the timing of expression of the thyroid hormone signaling pathway, a key molecular pathway that drives mouse PC dendritic maturation (41), was delayed relative to mouse PCs (Fig. 4*A*). This included delayed expression of *THRA*, *PPARGC1A*, and *RORα*. This observation is consistent with the slow time course of morphological maturation of hPSC-PCs relative to mouse PCs.

Second, we observed expression of a number of primate-specific genes that do not exist in the mouse genome (Fig. 4*B*). Primate-specific genes marked both early and late stages of hPSC-PC differentiation. *MICA*, *ZNF93*, *NBPF10*, *TMEM99*, *SMN2*, *NOTCH2NL*, *HHLA3*, and *CBWD2* were expressed at higher levels at day 24 than at day +95. *GTF2H2C*, *CBWD6*, and *DHRS4L2* were expressed at relatively similar levels at each time point. *RAB6C*, *ZNF90*, *GLUD2*, *POTEM*, *POTEE*, and *MT1M* were all up-regulated over differentiation from day 24 to day +95. While the roles of many of these genes unclear, *NOTCH2NL* and *GLUD2* have been linked to human-specific changes in brain development (42–48).

Third, we identified genes that are highly up-regulated in hPSC-PCs over differentiation but are not detected in postnatal mouse PCs (Fig. 4*C*). These included *CD40LG*, *SCN7A*, *PLN*, *CCDC178*, and *GIMAP4*. We further investigated expression of *CD40LG*, for which antibodies exist to confirm protein expression by immunolabeling. Immunolabeling of hPSC-PCs at day +90 and mouse PCs at P7 and P21 confirmed our transcriptomic data, showing colocalization of CD40LG with CALB1 in hPSC-PCs but not mouse PCs (Fig. 4*D* and *SI Appendix*, Fig. S4*D*). To verify that CD40LG is expressed in human PCs and not just hPSC-PCs, we labeled newborn human cerebellar tissue. Positive immunolabeling in CALB1$^+$ human PCs confirmed that our hPSC-PC model system had captured a species difference in gene expression and identified a novel human-specific PC marker (Fig. 4*D* and *SI Appendix*, Fig. S4*C*).

Discussion

To provide a more robust model for human PC differentiation, we optimized a protocol to generate hPSC-PCs. A key element of this protocol was the use of magnetic activated cell sorting (MACS) to purify immature hPSC-PCs, followed by coculturing the cells with mouse cerebellar glia and then, mouse GCs. With this methodology, hPSC-PCs had a more differentiated morphology, formed SYN1$^+$ synapses with mouse GCs, and fired large calcium

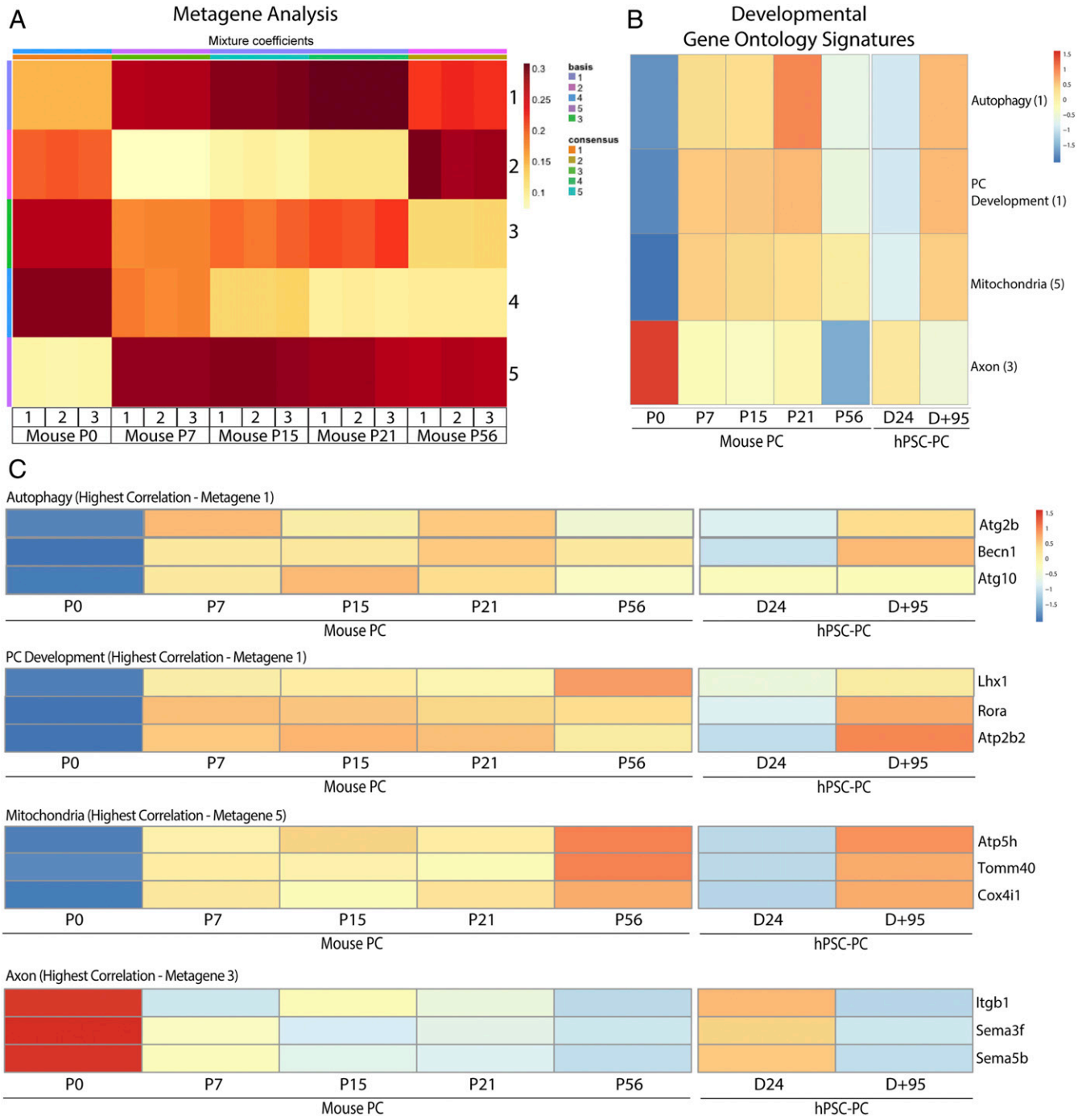

Fig. 3. NMF analysis of mouse PC developmental gene expression and comparison with hPSC-PCs. (*A*) Metagenes defined by NMF analysis of mouse PC gene expression over postnatal development. (*B*) GO expression signatures with a correlation coefficient to a metagene in *A* of >0.85. Listed next to the terms is the metagene with highest correlation. (*C*) Expression patterns of representative genes from each of the major GO categories found in *B*.

currents, measured with the genetically encoded calcium indicator jRGECO1a. To directly compare global gene expression of hPSC-PCs with developing mouse PCs, we used TRAP, expressing the Pcp2-L10a-Egfp TRAP tag in hPSCs. Comparison of key gene pathways between developing mouse PCs and differentiating hPSC-PCs revealed that differentiated hPSC-PCs are most similar to late juvenile (P21) mouse PCs, confirming the efficacy of the protocol in generating more differentiated PCs. Detailed comparison of global gene expression patterns of mouse PCs, using metagene projection analysis, showed that the key gene expression pathways of differentiated hPSC-PCs most closely matched those of late juvenile mouse PCs (P21). Comparative bioinformatics identified classical PC gene signatures as well as novel mitochondrial and autophagy gene pathways during the differentiation of both mouse and human PCs. In addition, we identified genes expressed in hPSC-PCs but not mouse PCs and confirmed protein expression of a novel human PC marker, CD40LG, expressed in both hPSC-PCs and native human cerebellar tissue. This study therefore provides a direct comparison of hPSC-PC and mouse PC gene expression and a robust method for generating differentiated hPSC-PCs

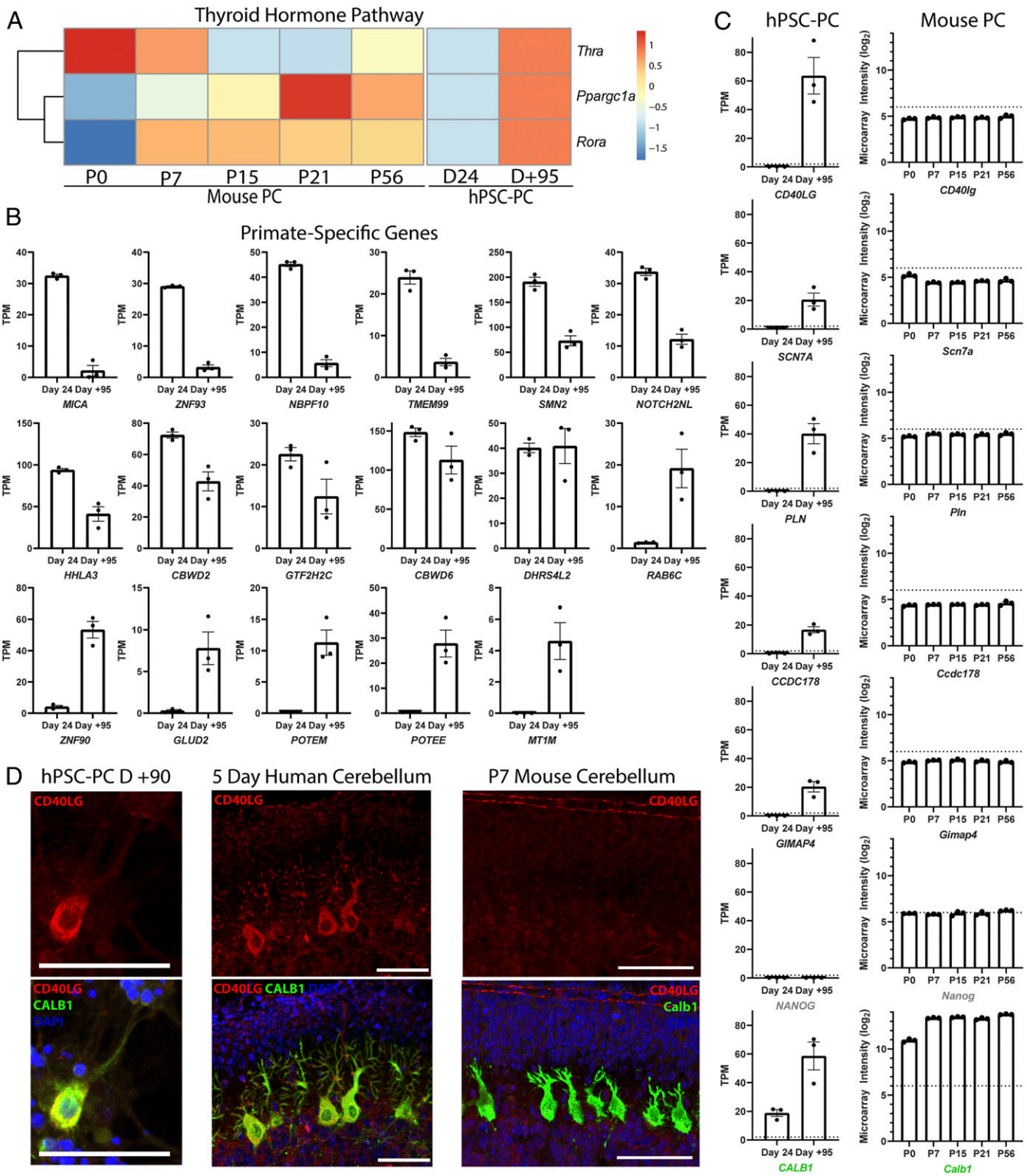

Fig. 4. Differences between hPSC-PCs and mouse PCs. (*A*) Expression patterns of thyroid hormone signaling pathway. (*B*) Expression levels of primate-specific genes in hPSC-PCs at day 24 and day +95. Error bars are SEM. (*C*) Expression levels of genes up-regulated in hPSC-PCs but not expressed in mouse PCs. For hPSC-PCs, background was set at 2 TPMs (dotted lines). For mouse PCs, background was set at microarray intensity of six (dotted lines). The negative control NANOG and the positive control CALB1 are shown for reference. Error bars are SEM. (*D*) Expression of CD40lg in hPSC-PCs and 5-d human cerebellum but not P7 mouse cerebellum. (Scale bars: 50 μm.)

with human-specific gene expression for modeling developmental and degenerative cerebellar disorders.

A wide range of studies has shown the importance of glia to hPSC–neuronal differentiation (49). For developing mouse PCs, Bergmann glia have been shown to grow in alignment with PC dendritic arbors, suggesting a role for glia in PC development (8). Here, we observed that coculturing hPSC-PCs with cerebellar glia prior to culturing them with presynaptic neurons appeared to promote differentiation as the cells expressed higher levels of the PC marker CALB1 and projected more complex dendrites after coculture with glia. In addition, cell–cell interactions with their synaptic partners, GCs, also appeared to promote PC differentiation. As discussed below, functional synaptic connections were necessary for hPSC-PC activity. These findings are consistent with the general observation that coculture of CNS neurons with glia and with target neurons promotes differentiation.

Expression of the genetically encoded calcium indicator jRGECO1a in hPSC-PCs was an efficient means to measure calcium currents in hPSC-PCs. Our observation that hPSC-PCs cocultured with mouse GCs fired calcium transients that could be blocked by TTX or CNQX is consistent with the interpretation that the hPSC-PCs were functionally active and had pharmacological properties of PCs. Many of the larger calcium responses showed a slow decay of 30 to 90 s, suggesting release of calcium from intracellular stores. This classical observation has been made in mouse PCs in cerebellar slices either by simultaneous activation of the climbing fiber and parallel fiber (50) or following train stimulation of parallel fibers only (51) and suggests strong activity in our cultures. In agreement with studies using calcium imaging in ex vivo slices, the dynamics of calcium imaging in our cocultures of hPSC-PCs and mouse GCs did not reveal simple spike activity. However, our results are consistent with the work of others (52) showing the utility of jRGECO1a to image PC somatic calcium, which provides a readout of average PC firing properties. Our findings support the interpretation that hPSC-PCs can fire action potentials and form synaptic connections with mouse GCs. Future studies utilizing electrophysiology will be necessary to properly define the physiological characteristics of hPSC-PCs.

One of the most consistent observations of hPSC-induced CNS neurons is the relatively slow and often incomplete maturation of human neurons (53). Our results suggest that a number of factors likely slow the development of human neurons. On a morphological level, the number of presynaptic inputs varies between human and mouse neurons. This feature is especially dramatic for PCs given the fact that the ratio of GC:PC inputs in human is almost 20-fold higher than mouse (54). This provides one possible explanation for the relatively immature dendritic arborization pattern of the hPSC-PCs we studied. In our experiments, by morphology, hPSC-PCs after ∼17 wk of differentiation resembled 18-wk human PCs (28). It will be interesting to determine whether bioengineering approaches to increase the density of GC:PC inputs also promote hPSC-PC dendritic density. Another possible reason hPSC-PCs are more immature is the fact that we cultured the cells for 4 mo, while native, human PCs mature over a 30-mo period. Finally, the timing of expression of the thyroid hormone gene pathway (*THRA1*, *RORα*, and *PPARGC1A*), which was shown by Heuer and Mason (41) to rapidly induce mouse PC differentiation beginning at P0, is not expressed until +95 d in vitro for hPSC-PCs, suggesting a possible molecular basis for delayed maturation of human PCs.

In contrast to the immature morphology we observed for hPSC-PCs, bioinformatic analysis of gene expression in hPSC-PCs and developing mouse PCs showed that hPSC-PCs most closely resembled late juvenile P21 mouse PCs. This finding suggests that the hPSC-PCs we studied are among the most mature hPSC-derived CNS neurons analyzed to date. This underscores the utility of transcriptomic analysis for analyzing the maturation of hPSC-derived CNS neurons. Our finding of shared PC signature gene sets in both mouse PC and hPSC-PC transcriptomes validates our conclusion of the identity of hPSC-PCs as Purkinje neurons.

Prior studies using metagene projection analysis have shown the efficacy of this approach for identifying the most salient features of gene expression pathways and for enabling cross-platform and cross-species analysis of gene expression in cancer (39) and in developing CNS neurons, including cerebellar GCs (40). In the present study, metagene analysis of global gene expression patterns of mouse PCs revealed classical PC signatures as well as novel mitochondria and autophagy pathways. These patterns were recapitulated in hPSC-PCs, suggesting that much of human and mouse PC development is conserved.

The finding that hPSC-PCs up-regulated mitochondrial gene sets after the formation of synapses with GCs and emergence of calcium firing properties is consistent with a role for mitochondria in calcium buffering and local, activity-driven protein synthesis in large output neurons (55). The importance of mitochondria to PCs has been well demonstrated in mouse models and is related directly or indirectly to many autosomal recessive cerebellar ataxias (56). Our findings identify P0 to P7 as the time when mitochondrial genes are highly up-regulated during mouse PC development and suggest that hPSC-PCs will be useful for studying human PC mitochondrial disorders.

The expression of autophagy gene sets by hPSC-PCs is also important for studies on degenerative cerebellar disorders. PCs are particularly affected in mice conditionally mutant for autophagy genes *Atg5* or *Atg7* (57, 58). In humans, a handful of congenital disorders of autophagy have been described, with mutations in *SNX14*, *ATG5*, and *SQSTM1/p62* affecting the cerebellum (59). Like mitochondria genes, our findings define P0 to P7 as the time when autophagy genes are up-regulated during mouse PC development. The coincidence in timing of mitochondrial and autophagy gene up-regulation raises the hypothesis that one key role for autophagy in PCs may be turnover of mitochondria, or mitophagy. Recent studies have found pathological roles for mitophagy in neurons in general and PCs specifically (60, 61). Up-regulation of autophagy genes in hPSC-PCs suggests that this model system will be useful for studying human PC autophagy disorders.

Translational profiling of hPSC-PCs and mouse PCs captured species-specific gene expression, consistent with findings of differential gene expression between human and rodent cerebellar cells (62). Two types of species-specific gene expression were observed, expression of primate-specific genes in hPSC-PCs that are nonexistent in mouse and up-regulation of genes in hPSC-PCs compared with background levels of expression in mouse PCs. Of the primate-specific genes, the roles of two genes in human neocortex development have recently been studied. *NOTCH2NL* is a human-specific paralog of the NOTCH receptor arising from gene duplication and contributing to expansion of cortical progenitors (42–44). *GLUD2* is a hominoidea-specific, intronless paralog of *Glud1*, arising from retroposition and contributing to changes in cortical gene expression and metabolism (45, 46). The roles of *NOTCH2NL*, *GLUD2*, and additional primate-specific genes in human PCs are unknown.

Of the genes expressed in hPSC-PCs but not expressed by mouse PCs, we found a sodium channel (*SCN7A*), a regulator of cardiac calcium flux (*PLN*), two genes with known roles in the immune system (*CD40LG* and *GIMAP4*), and a gene of unknown function (*CCDC178*). We further confirmed human-specific gene expression of CD40LG by immunofluorescence. CD40LG is well known for its expression in activated T cells (63), and a potential role in cortical neurite growth has been described (64). Further studies will be necessary to elucidate the function of this novel marker in human PCs and whether it serves a canonical "immune-like" or alternative role.

This study underscores the importance of genetic analysis of mouse and human CNS neurons for modeling CNS disease. Transcriptional profiling is a powerful methodology for confirming the identity of specific CNS neurons as well as for a quantitative measure of their state of differentiation. Future comparative studies on mouse and human neuronal transcriptomics and proteomics will provide insight on improving model systems for CNS neurological disease. To aid in disease modeling, human-specific features discovered in our study and others can be introduced into the mouse for more faithful recapitulation of human disease. These "humanized" mice will provide a complimentary system to hPSCs.

Materials and Methods

Contact for Reagent and Resource Sharing. Further information and requests for resources and reagents should be directed to and will be fulfilled by M.E.H.

Experimental Model and Subject Details.

Mice. Wild-type C57BL/6J mice (The Jackson Laboratory) were used for isolation of neonatal cerebellar glia cells and GCs (P5 to P7; see below for details). Isolated cells from both male and female pups were pooled. *Tg(Pcp2-L10a-Egfp)* TRAP mice were a gift from N. Heintz, The Rockefeller University, New York [also available from The Jackson Laboratory; B6; FVB-Tg(Pcp2-EGFP/Rpl10a) DR168Htz/J] (34). For isolation of PC TRAP RNA, cerebella were pooled from both male and female mice.

All mice were healthy and were housed with companion(s) in a specific pathogen-free animal facility in vented cages on a 12-h light/dark cycle. Food and water were provided ad libitum. All mouse experiments were performed in accordance with protocols approved by the Institutional Animal Care and Use Committee at The Rockefeller University.

Human embryonic stem cell culture and transgenesis. The RUES2 female human embryonic stem cell (hESC) line (a gift from A. Brivanlou, The Rockefeller University, New York) was maintained in mTeSR1 (Stem Cell Technologies; 85850) on hESC-qualified matrigel (Corning; 354277) at 37 °C with 5% CO_2 and subcultured weekly with ethylenediaminetetraacetic acid (EDTA) (Versene; ThermoFisher Scientific; 15040066) (65). Following karyotype analysis, cells were banked in mTeSR1 with 10% dimethyl sulfoxide in liquid nitrogen. Frozen stocks were thawed into mTeSR1 with 10 μM Y27632 (Stemgent; 04-0012-02) for the first day. Cells were used within five passages before thawing a new stock to avoid karyotype abnormalities. The RUES2-Pcp2-TRAP cell line was generated using lentiviral transduction (see below for details). All human embryonic stem cell studies were carried out in accordance with the Tri-Sci Embryonic Stem Cell Oversight Committee (Weill-Cornell Medical College, Memorial-Sloan Kettering Cancer Center, The Rockefeller University)-approved protocols.

Method Details.

Generation of RUES2-Pcp2-TRAP hESC line. Mouse pL7-mGFP (Pcp2-mGFP) plasmid was a gift from J. Hammer, NIH, Bethesda, MD (66). pC2-EGFP-L10a was a gift from N. Heintz. To subclone the L7 promoter into pC2-EGFP-L10a, oligonucleotides were used to insert a KpnI restriction site into the AseI restriction site of pC2-EGFP-L10a. The KpnI-AgeI fragment of pL7-mGFP containing ∼1 kb upstream through part of exon 4 of the mouse Pcp2 gene was subcloned into pC2-EGFP-L10a, replacing the cytomegalovirus promoter with L7. A PCR product was amplified from pL7-EGFP-L10a using the primers 5′-TTCAAAATT TTATCGATTAAGCTTCTCAGAGCATGGTCAG-3′ (forward) and 5′-AATAGGGCC CTCTAGATTATCTAGATCCGGTGGATCCC-3′ (reverse) containing ClaI and XbaI restriction sites. The PCR product was cloned into the linearized lentiviral vector pSIN-EF1a-promoter-BHH polyA-PGK-Puromycin, digested by ClaI and XbaI, using the In-Fusion HD Cloning Kit (Takara; 638909).

Lentivirus was produced by Lipofectamine 2000 (ThermoFisher; 11668030) transfection of ∼30 × 10^6 HEK293FT cells (ThermoFisher; R70007) with psPAX2 (6 μg), pMD2.G (2.5 μg), and pSIN-L7-EGFP-L10a (7 μg). Media were collected and filtered through a 0.45-μm polyvinylidene fluoride filter after 48 to 60 h, concentrated using the Lenti-X concentrator (Clontech; 631231), and stored at −80 °C.

Rues2 was dissociated to single cells and seeded at 70,000 cells per well of a Matrigel-coated 12-well plate in mTeSR1 with 10 μM Y27632 (Stemgent; 04-0012-02). The next day, 10 μl of lentiviral particles were added to fresh mTeSR1 medium containing 10 μM Y27632 and 4 μg/mL protamine sulfate (MilliporeSigma; P3369-10G). After 12 h, the cells were washed with phosphate-buffered saline (PBS) and fed with fresh mTeSR1 with 10 μM Y27632. After 48 h, transformed cells were selected by including 1 μg/mL puromycin (ThermoFisher; A1113803) in mTeSR1 with 10 μM Y27632. After an additional 48 h of selection, cells were dissociated to single cells, and 1,000 cells were seeded in a 10-cm dish in mTeSR1 with puromycin and Y27632 and maintained until colonies formed. Clonal lines were manually harvested and checked for normal karyotype (Memorial Sloan Kettering Cytogenetics Core) and for proper EGFP-L10a expression in $Pcp2^+$ cells by immunofluorescence following differentiation. RUES2-Pcp2-TRAP lines were maintained in mTeSR1 with puromycin when in the undifferentiated state with daily media changes. Puromycin was removed at the start of differentiation.

hESC differentiation. RUES2 maintained in mTeSR1 was dissociated into single cells using TrypLE (ThermoFisher; 12605010) and seeded in Dulbecco's Modified Eagle Medium/Nutrient Mixture F-12 (DMEM/F12) (ThermoFisher; 10565-018) with 1× nonessential amino acid (NEAA) (ThermoFisher; 11140050), 1× N-2 (ThermoFisher; 17502048), 1× B-27 (ThermoFisher; 12587010), 2 μg/mL heparin (MilliporeSigma; H3149), 1× Primocin (Invivogen; ant-pm-1), 10 mM nicotinamide (MilliporeSigma; N0636), 50 ng/mL noggin (Peprotech; 120-10C), 1.5 μM CHIR99021 (Stemgent; 04-0004-02), and 10 μM Y27631 (Stemgent; 04-0012-02) at 4,000 cells per 25 μL per well in an untreated 96-well V-bottom plate (ThermoFisher; 12-565-481). Cells were centrifuged for 5 min at 1,000 rpm to promote aggregate formation. For optimal differentiation efficiency, pluripotent cultures should be free of all differentiation, at 50 to 75% confluence, and cultured for 6 to 8 d after last passage. It should be noted that mTeSR1 contains LiCl, a GSK3β inhibitor, that likely activates some level of Wnt signaling. If undifferentiated cells are cultured in a different pluripotency medium, the concentration of CHIR99021 may need to be altered for proper midbrain/hindbrain specification.

On day 2 of differentiation, 175 μL per well of DMEM/F12 with 1× NEAA, 1× N-2, 1× B-27, 2 μg/mL heparin, 1× Primocin, 10 mM nicotinamide, 10 ng/mL noggin, and 1.5 μM CHIR99021 was added to the 96-well plate. On days 4 and 5, 175 μL per well of medium was replaced with 175 μL per well DMEM/F12 with 1× NEAA, 1× N-2, 1× B-27, 2 μg/mL heparin, 1× Primocin, and 100 ng/mL FGF8b (Peprotech; 100-25).

On day 6, aggregates are plated on laminin-coated (ThermoFisher; 27015; 10 μg/mL coated overnight at 37 °C) six-well tissue culture plates or laminin/poly-D-lysine–coated glass coverslips (NeuVitro; GG-12-1.5-pdl). Media (DMEM/F12 with 1× NEAA, 1× N-2, 1× B-27, 2 μg/mL heparin, 1× Primocin, 100 ng/mL FGF8b) were changed at 2 mL per well for 6-well plates or 0.5 mL per well for 12-well plates with 12-mm coverslips. Full media changes were performed on days 8 and 10 using the same media composition and volume.

On day 12, the basal medium was changed to neurobasal (ThermoFisher; 21103049), 1× Glutamax-I (ThermoFisher; 35050061), 1× N-2, 1× B-27, 1× Primocin, and 10 ng/mL BDNF (Peprotech; 450-02). Media were subsequently changed every other day using the same composition until isolation of PCs.

After 22 to 28 d of differentiation, postmitotic PCs were isolated and cocultured with mouse cerebellar glial cells. To isolate PCs, differentiated cultures were dissociated by incubating with 0.6 mg/mL Papain (Worthington Biochemical; LS003118) in calcium–magnesium-free PBS (dPBS; ThermoFisher; 14190-250; 0.2% glucose; MilliporeSigma; G8769; 0.004% sodium bicarbonate; MilliporeSigma; S8761-100ML; 0.00025% Phenol Red; MilliporeSigma; P0290) with 0.23 mg/mL L-cysteine (MilliporeSigma; C8277) for 30 min at 37 °C. Cell clumps were allowed to collect in the bottom of conical tubes, and excess papain was removed; 250 μL 0.5 mg/mL deoxyribonuclease (DNase) (Worthington Biochemical; LS002139; in Basal Medium Eagle [BME]; ThermoFisher; 21010-046 with 0.33% glucose) was added, and clumps were incubated at 37 °C for 5 min. Cell clumps in DNase were gently triturated with three decreasing bore sizes of fire-polished Pasteur pipettes until mostly single cells. Dissociated cells were passed through a 40-μm cell strainer (ThermoFisher; 352340), washed with 10 mL BME with 10% horse serum (ThermoFisher; 26050-088), and centrifuged for 5 min at 1,100 rpm.

Cells were resuspended in 5 mL CMF-PBS with 3% bovine serum albumin (BSA) (MilliporeSigma; A9576-50 mL), plated on anti-GD3 (Biolegend; 917701) 10-cm plates (untreated plates coated overnight at 4 °C with 13 μg GD3 antibody in 10 mL 50 mM Tris·HCl, pH 9.5; 1 10-cm GD3 plate per six-well dish of differentiated stem cells; washed 3× PBS before using), and incubated at room temperature for 20 min. Plates were tapped to dislodge partially attached cells, and the supernatant was transferred to another GD3 plate for an additional 20-min room temperature incubation. Plates were tapped to dislodge partially attached cells, and the supernatant was collected and centrifuged for 5 min at 1,100 rpm.

Cells were resuspended in 5 mL neural differentiation medium (BME; ThermoFisher; 21010-046; 1× N-2, 1× B-27, 0.9% BSA; MilliporeSigma; A9576-50 mL; 0.9% glucose; MilliporeSigma; G8769; 008% NaCl; 30 nM T3; MilliporeSigma; S8761; 1× Primocin) with 10 ng/mL BDNF and incubated at 37 °C and 5% CO_2 for 1 h. This step allows reexpression of NCAM1, which is

cleaved by papain. Cells were collected and centrifuged for 5 min at 1,100 rpm.

Cells were resuspended in 90 μL CMF-PBS with 3% BSA and 10 μL CD56 neural cell adhesion molecule (NCAM) microbeads (MiltenyiBiotec; 130-050-401) per 10^7 cells and incubated at 4 °C for 15 min; 10 mL CMF-PBS with 3% BSA was added to wash, and cells were centrifuged at 1,100 rpm. Cells were resuspended in 500 μL CMF-PBS with 3% BSA and 10 μL DNase and applied to an MACS column per the manufacturer's directions (MiltenyiBiotec; 130-042-201). Eluted cells were plated as 90-μL droplets at 1×10^5 cells per centimeter^2 on poly-D-lysine coverslips (Neuvitro; GG-12-1.5-pdl; coated overnight with 10 ng/mL laminin) with 1×10^4 mouse cerebellar glia per centimeter^2 in 24-well plates. Following attachment (~1 h), 1 mL neural differentiation medium with 10 ng/mL BDNF was added per well, and coverslips were carefully flipped using fine forceps so that cells were between the bottom of the plate and the coverslip. Mixed cultures were maintained at 35 °C with 5% CO_2. Cultures were exchanged with 0.5 mL media once per week. After 65 to 70 d, coverslips were gently flipped right side up, and 1×10^6 mouse cerebellar GCs per centimeter^2 were added; 0.5 mL medium was subsequently exchanged every Monday and Friday, with 4 μM Ara-C (MilliporeSigma; C6645-100MG) added 1 wk after GC addition.

Isolation of mouse cerebellar glia cells and GCs. Mouse cerebellar glia cells and GCs were isolated as previously described (67). Briefly, cerebella from P5 to P7 mice were dissected, dissociated to single cells with trypsin and DNase (Worthington Biochemical; 3703 and 2139), and separated on a 35/60% percoll gradient, resulting in two layers of cells. The top layer contained glia, interneurons, and PCs. This layer was collected and plated on Matrigel in DMEM/F12 (ThermoFisher; 10565-018) with 1× NEAA (ThermoFisher; 11140050), 1× N-2 (ThermoFisher; 17502048), 1× B-27 (ThermoFisher; 12587010), 2 μg/mL heparin (MilliporeSigma; H3149), and 1× Primocin (Invivogen; ant-pm-1) with 10% horse serum (ThermoFisher; 26050-088). Glia were grown and passaged at least once before use to remove neurons and were cultured for up to two passages before coculture with hPSC-PCs as described above. The bottom layer of the percoll gradient contained granule cells and were added to hPSC-PC/glia cultures as described above.

Real-time qPCR. RNA was isolated using the RNeasy Plus mini kit (Qiagen; 74134). Complementary DNA (cDNA) was generated from 1 μg RNA using the iScript cDNA Synthesis Kit (Bio-Rad; 1708891). qPCR was carried out on a Roche LightCycler 480 (Roche; 05015278001) using the SYBR green method (Roche; 04707516001) in triplicate 10-μL reactions run in a 96-well plate using half the cDNA synthesis reaction per plate. The qPCR protocol was 95 °C for 5 min and 45 rounds of 95 °C for 15 s, 56 °C for 15 s, and 72 °C for 10 s followed by a melt curve analysis from 65 °C to 95 °C. Primer specificity was confirmed by melting temperature analysis and gel electrophoresis. Data were normalized to the geometric mean of the "housekeeping" genes: glyceraldehyde phosphate dehydrogenase (*GAPDH*), hydroxymethylbilane synthase (*HMBS*), and glucose phosphate isomerase (*GPI*) (68). Primer sequences are listed in *SI Appendix*, Table S1.

Immunofluorescence labeling. Cells were fixed with 4% paraformaldehyde (Electron Microscopy Sciences; 15710) in dPBS (ThermoFisher; 14190-250) for 10 min at room temperature. In some instances, samples were embedded in O.C.T. medium (Electron Microscopy Sciences; 62550-01) and sectioned on a Leica CM3050S cryostat. Mouse cerebella and thymus were fixed in 4% paraformaldehyde in dPBS overnight at 4 °C and cut into 50-μm sections on a Leica VT1000S vibratome.

Samples were blocked in dPBS with 5% BSA and 1% donkey serum (Jackson Immunoresearch; 017-000-001). Concentration of primary antibodies and percentage Triton X-100 are listed in *SI Appendix*, Table S2. Primary antibodies were incubated overnight at 4 °C. After washing with PBS, appropriate secondary Alexa Fluor antibodies (Thermofisher) were incubated at 1:500 for 1 h at 4 °C. In some instances, DAPI was added for 5 min at room temperature before final washing in PBS. Coverslips were mounted in Fluoro-Gel (Electron Microscopy Sciences; 17985-10) and sealed with nail polish. Images were captured on an inverted Zeiss Axio Observer Z1 laser scanning confocal microscope.

Seven-micrometer paraffin sections of human 5-d cerebellum and human tonsil were rehydrated and treated with Trilogy solution (Cell Marque; 920P-04) in a conventional steamer for 40 min, followed by 20-min cooldown at room temperature. Sections were blocked for 2 h at room temperature in 10% normal goat serum, 1% BSA, and 0.1% Triton X-100 in PBS, pH 7.4, and then incubated overnight at 4 °C with mouse monoclonal anti-CD154 (1:50; R&D systems; MAB617) and rabbit anticalbindinD28k (1:500; Swant) in antibody diluent (1% BSA, 0.1% Triton X-100 in PBS, pH 7.4). Sections were washed three times in PBS–0.1% Tween followed by incubation for 2 h at room temperature in antibody diluent with anti-mouse and anti-rabbit goat secondary antibodies conjugated to Alexa Fluor 568 and Alexa Fluor 488, respectively (Invitrogen). After three washes in PBS–0.1% Tween, sections were mounted in DAPI Fluoromount-G (SouthernBiotech; 0100-01). Samples were collected at Columbia University Irvine Medical Center with previous patient consent and in strict accordance with institutional and legal ethical guidelines. Patient slides were deidentified prior to use in this study.

Flow cytometry. Differentiated cultures at day 24 were rapidly dissociated using Accumax (Innovative Cell Technologies; AM105) with 200 μL DNase (Worthington Biochemical) and 6 μL Far Red Fixable Dead Cell Stain (ThermoFisher; L34973) per 6 mL Accumax for 5 min at 37 °C followed by trituration with fire-polished Pasteur pipettes. Cell were spun down for 5 min at 1,100 rpm (4 °C) and resuspended in 4% paraformaldehyde (Electron Microscopy Sciences). Cells were fixed for 5 min at room temperature, washed, and resuspended in PBS. Rapid dissociation is necessary to retain strong PCP2 signal but not ideal for long-term cell culture.

Cells were blocked for 1 h at room temperature with block (5% BSA, 1% normal donkey serum, 0.05% Triton X-100 in PBS); 1×10^6 cells per condition were spun down and resuspended in primary antibody (anti-human L7/PCP2; Takara; M202, 1:500) or block (secondary only control) and incubated for 20 min on ice. Cells were spun down, washed once with 2 mL block, resuspended in secondary antibody (donkey anti-rabbit Alexa Fluor 488; ThermoFisher; 1:500), and incubated for 20 min on ice. Cells were washed again with 2 mL block and resuspended in 200 μL PBS. In control experiments, Far Red Fixable Dead Cell Stain was left out of the dissociation, and fixed cells were labeled with DRAQ5 (Biolegend; 424101) at 1:500 for 10 min at room temperature in the dark to label nuclei.

Day 24 cells were analyzed on a BD Accuri C6 flow cytometer. Cells were gated for single cells using DRAQ5-labeled cells and forward scatter (FSC) area vs. height for doublet discrimination. Dead cells were gated out according to Far Red Fixable Dead Stain labeling, which comprised ~7 to 8% of the population. Cells were considered positive if the fluorescence was greater than 0.01% of the secondary-only control.

TRAP RNA isolation. TRAP RNA was isolated as previously described (31, 40, 69). Briefly, for *Tg(Pcp2-L10a-Egfp)* mice, pooled cerebella were immediately homogenized with a Teflon-glass homogenizer in ice-cold polysome extraction buffer (10 mM Hepes-KOH, pH 7.4, 150 mM KCl, 5 mM $MgCl_2$, 0.5 mM dithiothreitol (MilliporeSigma; D9779-1G), 100 μg/mL cycloheximide (MilliporeSigma; C7698-1G), Superasin and RNasin RNase inhibitors (ThermoFisher; AM2694, PR-N2515), and complete EDTA-free protease inhibitor (MilliporeSigma; 11836170001). Following clearing by centrifugation, supernatants were incubated at 4 °C with end-over-end rotation for 16 to 18 h with biotinylated Streptavidin T1 Dynabeads (ThermoFisher; 65601) previously conjugated with GFP antibodies (Sloan Kettering Institute Antibody Core; HtzGFP-19C8 and HtzGFP-19F7). The beads were collected on a magnetic rack, washed, and resuspended in lysis buffer with β-mercaptoethanol (Agilent; 400753) to extract bound RNA from polysomes. RNA was purified using the Stratagene Absolutely RNA Nanoprep kit (Agilent; 400753). For RUES2-Pcp2-TRAP hPSC-PCs, polysomes were stabilized by adding 100 μg/mL cycloheximide to cell culture media for 10 min prior to homogenization with polysome extraction buffer and isolation as described above. RNA was purified using the RNeasy micro kit (Qiagen; 74004). RNA quantity and quality were measured using an Agilent 2100 Bioanalyzer with the 6000 Pico Kit (Agilent; 5067-1513).

Microarray. Microarray experiments were performed as previously described (40). Briefly, purified RNA was amplified using the SuperScript GeneChip Expression 3′-Amplification Reagents Two-Cycle cDNA Synthesis Kit (Affymetrix) and the GeneChip T7-Oligo Primer (Affymetrix). The cDNA was used for the in vitro synthesis of complementary RNA (cRNA) using the MEGAscriptT7 Kit (Ambion). cRNA was purified using the GeneChip Sample Cleanup Module (Affymetrix); 600 ng or less of clean cRNA was used in the second-cycle cDNA synthesis reaction using the SuperScript GeneChip Expression 3′-Amplification Reagents Two-Cycle cDNA Synthesis Kit (Affymetrix) and random primers (Affymetrix). The cDNA was purified using the GeneChip Sample Cleanup Module (Affymetrix). Purified cDNA was used for the in vitro synthesis of biotin-labeled cRNA using the GeneChip IVT Labeling Kit (Affymetrix). cRNA was purified using the GeneChip Sample Cleanup Module (Affymetrix) and fragmented into 35- to 200-base pair fragments using a magnesium acetate buffer (Affymetrix). Ten micrograms of labeled cRNA was hybridized to Affymetrix GeneChip Mouse Gene 1.0 ST Array for 16 h at 45 °C. The GeneChips were washed and stained according to the manufacturer's recommendations (Affymetrix) using the GeneChips Fluidics Station 450 (Affymetrix). Mouse Gene 1.0 ST arrays were scanned using the GeneChip Scanner 3000 (Affymetrix).

RNA sequencing. One nanogram of total RNA was used to generate full-length cDNA using Clontech's SMART-Seq v4 Ultra Low Input RNA Kit (catalog no. 634888); 1 ng of cDNA was then used to prepare libraries using the Illumina

Nextera XT DNA sample preparation kit (catalog no. FC-131-1024). Libraries with unique barcodes were pooled at equal molar ratios and sequenced on an Illumina NextSeq 500 sequencer to generate 75-base pair single reads, following the manufacturer's protocol (catalog no. 15048776 Rev.E).

Calcium imaging. To image calcium spikes in hPSC-PCs, postmitotic cells were nucleofected during the isolation step of the differentiation protocol (after 22 to 28 d). Following GD3-negative immunopanning, the semipurified mixture of cells was nucleofected with 2 μg/10^6 cells of each: pL7-mGFP [Pcp2-mGFP; gift from J. Hammer (66)] and jRGECO1a [pAAV.Syn.NES-jRGECO1a.WPRE.SV40; gift from Douglas Kim and GENIE Project (Ashburn, Virginia); Addgene plasmid no. 100854 (30)]. Nucleofection was performed on an Amaxa nucleofector IIb using protocol O-003 with the mouse neuron kit (Lonza; VPG-1001). Cells were allowed to recover for 1 h at 37 °C and followed by NCAM1 MACS and culture as described above.

Following isolation and nucleofection, cells were cultured with mouse cerebellar glia for 70 d and then, mouse cerebellar GCs for an additional 30 d. To record changes in fluorescence over time, cells expressing both jRGECO1a and GFP were recorded by an Andor iXon 512 × 512 electron multiplying charged coupled device (EMCCD) camera using an inverted Zeiss Axiovert 200 with a Perkin-Elmer UltraView spinning disk confocal head. Images were captured at 3.47 Hz for a total of 143.712 s per recording. Baseline recordings on day +100 were made from 23 cells from three separate culture dishes; 25 μM CNQX was added, and recordings were made from 15 cells from three separate culture dishes. CNQX was washed out, and media were replaced. On day 101, baseline recordings were made to confirm activity before adding 300 nM TTX (Tocris; 1078). Recordings were made from 10 cells from three separate culture dishes. TTX was washed out, and resumption of calcium activity was confirmed.

To analyze recordings, files were opened with ImageJ (NIH), and integrated density from an individual cell was analyzed over time. F_o was set as the lowest integrated density over the recording. Traces of $\Delta F/F_o$ in Fig. 1*I* and *SI Appendix*, Fig. S1*C* are representative traces of various calcium firing patterns we observed. Traces in Fig. 1 *J* and *K* are representative traces in the presence of synaptic inhibitors. No spikes were ever observed in the presence of synaptic inhibitors. To quantify the number of active cells, $\Delta F/F_o > 0.3$ was considered active. This baseline was chosen because it was reported that rat hippocampal neurons firing a single-action potential had an average $\Delta F/F_o$ of 0.3 (30). Eight cells were recorded each from three separate dishes.

Quantification and Statistical Analysis.

qPCR analysis. Three biological replicates for each differentiation condition were analyzed. Relative gene expression levels were normalized to the geometric mean of the housekeeping genes: *GAPDH*, *HMBS*, and *GPI* (68). Student's *t* test was used for statistical comparison between two groups using GraphPad Prism software.

Immunocytochemistry quantification. For quantification of EN1/OTX2 at day 6, images of four individual neural aggregates were quantified for EN1, OTX2, and DAPI using ImageJ. For quantification of GFP/PCP2 at day 24, images from three biological replicates were quantified for GFP and PCP2 using ImageJ. For quantification of PCP2/hNUC at day 95, four images each from three separate coverslips were quantified for PCP2 and hNUC using ImageJ.

Microarray analysis. Microarray data were normalized using robust multiarray average methods implemented in Affymetrix Power Tools (70), and changes between functional groups were assessed using the Limma Bioconductor package (71). Clustering of mouse transcriptome profiles was performed using NMF implemented in the NMF package (72). ssGSEA analysis was performed using the GSVA Bioconductor package (36) with query gene sets retrieved from MsigDB databases (73) or derived as Gene Matrix Transposed file format from the human RNAseq data.

RNA sequencing analysis. Sequence and transcript coordinates for human hg19 University of California, Santa Cruz (UCSC) genome and gene models were retrieved from the Bioconductor Bsgenome.Hsapiens.UCSC.hg19 and TxDb.Hsapiens.UCSC.hg19.knownGene libraries, respectively. Unaligned sequence reads were retrieved as FastQ format. FastQ files for day 24 samples were down sampled using the ShortRead R package to equilibrate total mapped reads to day 95 samples. Transcript expression was calculated using the Salmon software quantification (74), and gene expression levels as transcripts per million (TPMs) and counts were retrieved using Tximport (75). Differential gene expression analysis was performed using DESeq2 (76). For visualization in genome browsers, RNAseq reads are aligned to the genome using Rsubread's subjunc method (77) and exported as bigWigs normalized to reads per million using the rtracklayer package.

To further assess any potential contamination by mouse feeder cells following human-specific immunoprecipitation, RNAseq data were aligned to an in silico combined genome (ISCG), and a conservative, mouse-subtracted, human transcriptome dataset was acquired (37). To create the ISCG, sequence and transcript coordinates for mouse mm10 UCSC genome and gene models were retrieved from the Bioconductor Bsgenome.Mmusculus.UCSC.mm10 and TxDb.Mmusculus.UCSC.mm10.knownGene libraries and combined with the above hg19 genome. RNAseq reads were then mapped to the ISCG with Subread, and gene expression estimates were acquired using Featurecounts and Salmon. Human-specific gene expression estimates were then retrieved from the ISCG estimates and used in differential gene expression performed with DEseq2.

Data and software availability. Microarray data can be found at https://www.ncbi.nlm.nih.gov/geo/ (accession no. GSE140307). RNAseq data can be found at https://www.ncbi.nlm.nih.gov/geo/ (accession no. GSE140306).

ACKNOWLEDGMENTS. We thank members of the laboratory of M.E.H. for helpful discussions; the Brivanlou laboratory and Stem Cell core (The Rockefeller University) for helpful discussions and reagents; Dr. Nathaniel Heintz (The Rockefeller University) for helpful discussions, TRAP(L10a-EGFP) plasmid, and TRAP mice *Tg(Pcp2-L10a-Egfp)*; Dr. John Hammer (NIH) for Pcp2-mGFP reporter plasmid; Dr. Thomas Jessell (Columbia University) for En1 antibody; Dr. Pablo Tamayo (University of California, San Diego) for helpful discussion about metagene analysis; Dr. Mustafa Sahin and Dr. Maria Sundberg (Boston Children's Hospital) for helpful discussions; summer students Maya Pandit, Lauren Cantor, and Victoria Marino; and The Rockefeller University Bio-Imaging, Genomics, Comparative Bioscience Center, Flow Cytometry, and Bioinformatics resource centers. This work was supported in part by Pilot Grant UL1TR001866 (to D.E.B. and M.E.H.) from the National Center for Advancing Translational Sciences (NIH Clinical and Translational Science Award program) administered by The Rockefeller University Center for Clinical and Translational Science; by National Institute of Neurological Disorders and Stroke Grant 1R21NS093540-01 (to M.E.H.); by Department of Defense US Army Medical Research Acquisition Activity Grants W81XWH1510189 (to M.E.H.) and W81XWH1910110 (to M.E.H.); by A-T Children's Project Grant HATTEN2018 (to M.E.H.); and by a Starr Tri-Institutional Stem Cell Initiative Grant (to M.E.H.) from the Starr Foundation 2016-001. H.B. and P.L.F. are both affiliated with Columbia University.

1. S. Marek *et al*., Spatial and temporal organization of the individual human cerebellum. *Neuron* **100**, 977–993.e7 (2018).
2. J. D. Schmahmann, The cerebellum and cognition. *Neurosci. Lett.* **688**, 62–75 (2019).
3. I. Carta, C. H. Chen, A. L. Schott, S. Dorizan, K. Khodakhah, Cerebellar modulation of the reward circuitry and social behavior. *Science* **363**, eaav0581 (2019).
4. S. H. Fatemi *et al*., Consensus paper: Pathological role of the cerebellum in autism. *Cerebellum* **11**, 777–807 (2012).
5. S. S. H. Wang, A. D. Kloth, A. Badura, The cerebellum, sensitive periods, and autism. *Neuron* **83**, 518–532 (2014).
6. P. T. Tsai *et al*., Autistic-like behaviour and cerebellar dysfunction in Purkinje cell Tsc1 mutant mice. *Nature* **488**, 647–651 (2012).
7. T. Ashizawa, G. Öz, H. L. Paulson, Spinocerebellar ataxias: Prospects and challenges for therapy development. *Nat. Rev. Neurol.* **14**, 590–605 (2018).
8. K. Leto *et al*., Consensus paper: Cerebellar development. *Cerebellum* **15**, 789–828 (2016).
9. A. D. Kloth *et al*., Cerebellar associative sensory learning defects in five mouse autism models. *eLife* **4**, e06085 (2015).
10. P. T. Tsai *et al*., Sensitive periods for cerebellar-mediated autistic-like behaviors. *Cell Rep.* **25**, 357–367.e4 (2018).
11. K. R. Choy, D. J. Watters, Neurodegeneration in ataxia-telangiectasia: Multiple roles of ATM kinase in cellular homeostasis. *Dev. Dyn.* **247**, 33–46 (2018).
12. J. A. Thomson, Embryonic stem cell lines derived from human blastocysts. *Science* **282**, 1145–1147 (1998). Erratum in: *Science* **282**, 1827 (1998).
13. K. Takahashi *et al*., Induction of pluripotent stem cells from adult human fibroblasts by defined factors. *Cell* **131**, 861–872 (2007).
14. J. Yu *et al*., Induced pluripotent stem cell lines derived from human somatic cells. *Science* **318**, 1917–1920 (2007).
15. K. Muguruma, A. Nishiyama, H. Kawakami, K. Hashimoto, Y. Sasai, Self-organization of polarized cerebellar tissue in 3D culture of human pluripotent stem cells. *Cell Rep.* **10**, 537–550 (2015).
16. S. Wang *et al*., Differentiation of human induced pluripotent stem cells to mature functional Purkinje neurons. *Sci. Rep.* **5**, 9232 (2015).
17. Y. Ishida *et al*., Vulnerability of Purkinje cells generated from spinocerebellar ataxia type 6 patient-derived iPSCs. *Cell Rep.* **17**, 1482–1490 (2016).
18. M. Sundberg *et al*., Purkinje cells derived from TSC patients display hypoexcitability and synaptic deficits associated with reduced FMRP levels and reversed by rapamycin. *Mol. Psychiatry* **23**, 2167–2183 (2018).
19. H. Wichterle, I. Lieberam, J. A. Porter, T. M. Jessell, Directed differentiation of embryonic stem cells into motor neurons. *Cell* **110**, 385–397 (2002).
20. S. M. Chambers *et al*., Highly efficient neural conversion of human ES and iPS cells by dual inhibition of SMAD signaling. *Nat. Biotechnol.* **27**, 275–280 (2009).
21. D. E. Buchholz *et al*., Rapid and efficient directed differentiation of human pluripotent stem cells into retinal pigmented epithelium. *Stem Cells Transl. Med.* **2**, 384–393 (2013).

22. Y. Meng *et al*., Nicotinamide promotes cell survival and differentiation as kinase inhibitor in human pluripotent stem cells. *Stem Cell Rep.* **11**, 1347–1356 (2018).
23. S. Kriks *et al*., Dopamine neurons derived from human ES cells efficiently engraft in animal models of Parkinson's disease. *Nature* **480**, 547–551 (2011).
24. A. Kirkeby *et al*., Generation of regionally specified neural progenitors and functional neurons from human embryonic stem cells under defined conditions. *Cell Rep.* **1**, 703–714 (2012).
25. J. Xi *et al*., Specification of midbrain dopamine neurons from primate pluripotent stem cells. *Stem Cells* **30**, 1655–1663 (2012).
26. A. L. Garda, D. Echevarría, S. Martínez, Neuroepithelial co-expression of Gbx2 and Otx2 precedes Fgf8 expression in the isthmic organizer. *Mech. Dev.* **101**, 111–118 (2001).
27. C. A. Baptista, M. E. Hatten, R. Blazeski, C. A. Mason, Cell-cell interactions influence survival and differentiation of purified Purkinje cells in vitro. *Neuron* **12**, 243–260 (1994).
28. N. Zecevic, P. Rakic, Differentiation of Purkinje cells and their relationship to other components of developing cerebellar cortex in man. *J. Comp. Neurol.* **167**, 27–47 (1976).
29. P. Rakic, R. L. Sidman, Histogenesis of cortical layers in human cerebellum, particularly the lamina dissecans. *J. Comp. Neurol.* **139**, 473–500 (1970).
30. H. Dana *et al*., Sensitive red protein calcium indicators for imaging neural activity. *eLife* **5**, e12727 (2016).
31. M. Heiman, R. Kulicke, R. J. Fenster, P. Greengard, N. Heintz, Cell type-specific mRNA purification by translating ribosome affinity purification (TRAP). *Nat. Protoc.* **9**, 1282–1291 (2014).
32. J. Oberdick, R. J. Smeyne, J. R. Mann, S. Zackson, J. I. Morgan, A promoter that drives transgene expression in cerebellar Purkinje and retinal bipolar neurons. *Science* **248**, 223–226 (1990).
33. Y. Serinagaoglu *et al*., A promoter element with enhancer properties, and the orphan nuclear receptor RORalpha, are required for Purkinje cell-specific expression of a Gi/o modulator. *Mol. Cell. Neurosci.* **34**, 324–342 (2007).
34. J. P. Doyle *et al*., Application of a translational profiling approach for the comparative analysis of CNS cell types. *Cell* **135**, 749–762 (2008).
35. X. Xia, Y. Zhang, C. R. Zieth, S.-C. Zhang, Transgenes delivered by lentiviral vector are suppressed in human embryonic stem cells in A promoter-dependent manner. *Stem Cells Dev.* **16**, 167–176 (2012).
36. S. Hänzelmann, R. Castelo, J. Guinney, GSVA: Gene set variation analysis for microarray and RNA-seq data. *BMC Bioinf.* **14**, 7 (2013).
37. M. Callari *et al*., Computational approach to discriminate human and mouse sequences in patient-derived tumour xenografts. *BMC Genom.* **19**, 19 (2018).
38. J. P. Brunet, P. Tamayo, T. R. Golub, J. P. Mesirov, Metagenes and molecular pattern discovery using matrix factorization. *Proc. Natl. Acad. Sci. U.S.A.* **101**, 4164–4169 (2004).
39. P. Tamayo *et al*., Metagene projection for cross-platform, cross-species characterization of global transcriptional states. *Proc. Natl. Acad. Sci. U.S.A.* **104**, 5959–5964 (2007).
40. X. Zhu *et al*., Role of Tet1/3 genes and chromatin remodeling genes in cerebellar circuit formation. *Neuron* **89**, 100–112 (2016).
41. H. Heuer, C. A. Mason, Thyroid hormone induces cerebellar Purkinje cell dendritic development via the thyroid hormone receptor α1. *J. Neurosci.* **23**, 10604–10612 (2003).
42. M. Florio *et al*., Evolution and cell-type specificity of human-specific genes preferentially expressed in progenitors of fetal neocortex. *eLife* **7**, e32332 (2018).
43. I. T. Fiddes *et al*., Human-specific NOTCH2NL genes affect notch signaling and cortical neurogenesis. *Cell* **173**, 1356–1369.e22 (2018).
44. I. K. Suzuki *et al*., Human-specific NOTCH2NL genes expand cortical neurogenesis through delta/notch regulation. *Cell* **173**, 1370–1384.e16 (2018).
45. P. Shashidharan, A. Plaitakis, The discovery of human of GLUD2 glutamate dehydrogenase and its implications for cell function in health and disease. *Neurochem. Res.* **39**, 460–470 (2014).
46. Q. Li *et al*., Mice carrying a human GLUD2 gene recapitulate aspects of human transcriptome and metabolome development. *Proc. Natl. Acad. Sci. U.S.A.* **113**, 5358–5363 (2016).
47. Y. Hahn, T. K. Bera, I. H. Pastan, B. Lee, Duplication and extensive remodeling shaped POTE family genes encoding proteins containing ankyrin repeat and coiled coil domains. *Gene* **366**, 238–245 (2006).
48. J. Young, J. Ménétrey, B. Goud, RAB6C is a retrogene that encodes a centrosomal protein involved in cell cycle progression. *J. Mol. Biol.* **397**, 69–88 (2010).
49. M. A. Johnson, J. P. Weick, R. A. Pearce, S. C. Zhang, Functional neural development from human embryonic stem cells: Accelerated synaptic activity via astrocyte coculture. *J. Neurosci.* **27**, 3069–3077 (2007).
50. A. Konnerth, J. Dreessen, G. J. Augustine, Brief dendritic calcium signals initiate long-lasting synaptic depression in cerebellar Purkinje cells. *Proc. Natl. Acad. Sci. U.S.A.* **89**, 7051–7055 (1992).
51. J. Eilers, H. Takechi, E. A. Finch, G. J. Augustine, A. Konnerth, Local dendritic Ca2+ signaling induces cerebellar long-term depression. *Learn. Mem.* **4**, 159–168 (1997).
52. J. E. Ramirez, B. M. Stell, Calcium imaging reveals coordinated simple spike pauses in populations of cerebellar Purkinje cells. *Cell Rep.* **17**, 3125–3132 (2016).
53. D. Cornacchia, L. Studer, Back and forth in time: Directing age in iPSC-derived lineages. *Brain Res.* **1656**, 14–26 (2017).
54. P. Haldipur, K. J. Millen, What cerebellar malformations tell us about cerebellar development. *Neurosci. Lett.* **688**, 14–25 (2019).
55. V. Rangaraju, M. Lauterbach, E. M. Schuman, Spatially stable mitochondrial compartments fuel local translation during plasticity. *Cell* **176**, 73–84.e15 (2019).
56. M. Synofzik, H. Puccio, F. Mochel, L. Schöls, Autosomal recessive cerebellar ataxias: Paving the way toward targeted molecular therapies. *Neuron* **101**, 560–583 (2019).
57. T. Hara *et al*., Suppression of basal autophagy in neural cells causes neurodegenerative disease in mice. *Nature* **441**, 885–889 (2006).
58. M. Komatsu *et al*., Loss of autophagy in the central nervous system causes neurodegeneration in mice. *Nature* **441**, 880–884 (2006).
59. D. Ebrahimi-Fakhari, Congenital disorders of autophagy: What a pediatric neurologist should know. *Neuropediatrics* **49**, 18–25 (2018).
60. S. H. Kuo *et al*., Macroautophagy abnormality in essential tremor. *PLoS One* **7**, e53040 (2012).
61. D. Ebrahimi-Fakhari *et al*., Impaired mitochondrial dynamics and mitophagy in neuronal models of tuberous sclerosis complex. *Cell Rep.* **17**, 1053–1070 (2016).
62. X. Xu *et al*., Species and cell-type properties of classically defined human and rodent neurons and glia. *eLife* **7**, e37551 (2018).
63. R. J. Armitage *et al*., Molecular and biological characterization of a murine ligand for CD40. *Nature* **357**, 80–82 (1992).
64. P. Carriba, A. M. Davies, CD40 is a major regulator of dendrite growth from developing excitatory and inhibitory neurons. *eLife* **6**, e30442 (2017).
65. J. Beers *et al*., Passaging and colony expansion of human pluripotent stem cells by enzyme-free dissociation in chemically defined culture conditions. *Nat. Protoc.* **7**, 2029–2040 (2012).
66. W. Wagner, S. McCroskery, J. A. Hammer 3rd, An efficient method for the long-term and specific expression of exogenous cDNAs in cultured Purkinje neurons. *J. Neurosci. Methods* **200**, 95–105 (2011).
67. M. E. Hatten, Neuronal regulation of astroglial morphology and proliferation in vitro. *J. Cell Biol.* **100**, 384–396 (1985).
68. M. J. Radeke, K. E. Peterson, L. V. Johnson, D. H. Anderson, Disease susceptibility of the human macula: Differential gene transcription in the retinal pigmented epithelium/choroid. *Exp. Eye Res.* **85**, 366–380 (2007).
69. A. Kocabas, T. Duarte, S. Kumar, M. A. Hynes, Widespread differential expression of coding region and 3′ UTR sequences in neurons and other tissues. *Neuron* **88**, 1149–1156 (2015).
70. R. A. Irizarry *et al*., Exploration, normalization, and summaries of high density oligonucleotide array probe level data. *Biostatistics* **4**, 249–264 (2003).
71. M. E. Ritchie *et al*., Limma powers differential expression analyses for RNA-sequencing and microarray studies. *Nucleic Acids Res.* **43**, e47 (2015).
72. R. Gaujoux, C. Seoighe, A flexible R package for nonnegative matrix factorization. *BMC Bioinf.* **11**, 367 (2010).
73. A. Subramanian *et al*., Gene set enrichment analysis: A knowledge-based approach for interpreting genome-wide expression profiles. *Proc. Natl. Acad. Sci. U.S.A.* **102**, 15545–15550 (2005).
74. R. Patro, G. Duggal, M. I. Love, R. A. Irizarry, C. Kingsford, Salmon provides fast and bias-aware quantification of transcript expression. *Nat. Methods* **14**, 417–419 (2017).
75. M. I. Love, J. B. Hogenesch, R. A. Irizarry, Modeling of RNA-seq fragment sequence bias reduces systematic errors in transcript abundance estimation. *Nat. Biotechnol.* **34**, 1287–1291 (2016).
76. M. I. Love, C. Soneson, R. Patro, Swimming downstream: Statistical analysis of differential transcript usage following Salmon quantification. *F1000 Res.* **7**, 952 (2018).
77. Y. Liao, G. K. Smyth, W. Shi, The Subread aligner: Fast, accurate and scalable read mapping by seed-and-vote. *Nucleic Acids Res.* **41**, e108 (2013).